Microscale Updrafts Within Northeast U.S. Coastal Snowstorms Using High-Resolution Cloud Radar Measurements

Mariko Oue[1], Brian A. Colle[1], Sandra E. Yuter[2], Pavlos Kollias[1,3], Phillip Yeh[1], Laura M. Tomkins[2],

1. *Stony Brook University, Stony Brook, NY*
2. *North Carolina State University*
3. *Brookhaven National Laboratory*

Corresponding author: Mariko Oue, mariko.oue@stonybrook.edu

ABSTRACT

Limited knowledge exists about ~100 m scale precipitation processes within U.S. Northeast coastal snowstorms because of a lack of high-resolution observations. We investigate characteristics of microscale updraft regions within the cyclone comma head and their relationships with snowbands, wind shear, frontogenesis, and vertical mass flux using high-spatiotemporal resolution vertically-pointing Ka-band radar measurements, soundings, and reanalysis data for four snowstorms observed at Stony Brook, NY. Updraft regions are defined as contiguous time-height plotted areas with upward Doppler velocity without hydrometeor sedimentation that is equal to or greater than 0.4 m s^{-1}. Most updraft regions in the time-height data occur on a time scale of seconds (< 20 s), which is equivalent to spatial scales < 500 m. These small updraft regions within cloud echo occur more than 30% of the time for three of the four cases and 18% for the other case. They are found at all altitudes and can occur with or without frontogenesis and with or without snowbands. The updraft regions with relatively large Doppler spectrum width (> 0.4 m s^{-1}) occur more frequently within midlevels of the storms, where there are strong wind shear layers and moist shear instability layers. This suggests that the dominant forcing for the updrafts appears to be turbulence associated with the vertical shear instability. The updraft regions can be responsible for upward mass flux when they are closer together in space and time. The higher values of mean upward mass flux within updraft regions often occur during snowband periods.

SIGNIFICANCE STATEMENT

Small-scale (< 500 m) upward motions within four snowstorms along the U.S. Northeast Coast are analyzed for the first time using high spatiotemporal resolution millimeter-wavelength cloud radar pointed vertically. The analysis reveals these updrafts appear in the storms regardless of whether snowbands are present or whether there is larger-scale forcing for ascent. The more turbulent and stronger updrafts frequently occur in midlevels of storms associated with instability from vertical shear and contribute to upward mass flux during snowband periods when they are closer together in space and time.

1. Introduction

Snowbands in the comma head of winter storms are responsible for much of the heavy snowfall over the northeast United States. Because of the large societal impacts of these winter storms, they have been studied for decades using both numerical models and observations (e.g., Novak et al. 2008; Stark et al. 2013; Plummer et al. 2014; McMurdie et al. 2022). These studies have shown a spectrum of snowbands, ranging from single bands, which are defined as a single reflectivity feature > 250 km in length, 20–100 km in width, and with intensities of > 30 dBZ maintained for at least 2 hours, to smaller-scale multibands that occur in groups (Ganetis et al. 2018). The mechanisms that result in the variations in snowband characteristics are not well known.

Previous studies on snowband formation focused on the mesoscale ingredients of lift along a mid-level trough, instability, and moisture (Novak et al. 2010). While primary bands were often associated with mid-level frontogenesis (e.g., Novak et al. 2004, 2008), multibands were also associated with mesoscale instabilities, such as boundary layer instability, moist/conditional symmetric instability (e.g., Byrd 1989; Schultz and Schumacher 1999), conditional instability (e.g., Reuter and Yau 1990; Trapp et al. 2001; Morales 2008) and inertial instability (e.g., Jurewicz and Evans 2004; Schultz and Knox 2007). Earlier modeling and theoretical studies of multibands focused on the superposition of a frontogenetical circulation and either conditional instability or conditional symmetric instability (Xu 1992). However, Ganetis et al. (2018) showed that these bands often develop in a region of little or no frontogenesis; thus, other mechanisms may be responsible, such as elevated convection, generating cells, shear instabilities, and gravity wave activity, as well as microphysics, which often occur at smaller scales than frontogenesis and mesoscale instabilities (Bosart and Sanders 1986; Zhang et al. 2001, 2003; Kumjian et al. 2014; Plummer et al. 2014, 2015; Rauber et al. 2014, 2017; Rosenow et al. 2014, 2018; Keeler et al. 2016a, b, 2017; Kumjian and Lombardo 2017; Lackmann and Thompson 2019; McMurdie et al. 2022).

Snowbands also have variable microphysics that can impact precipitation rates. Studies using in-situ surface measurements observed a variety of snowflake habits and degrees of riming within the cyclone comma head and storm evolution (e.g., Stark et al. 2013; Colle et al., 2014). In particular, the microphysical processes can change across the snowband from more rimed on the east (warmer) side to more dry snow on the west (colder) side. Those microphysical studies using

76 in-situ surface measurements have also revealed that upper-level cloud structures, dynamics, and
77 microphysics (i.e., generating cells, turbulence) strongly impact the surface precipitation, while
78 internal cloud processes can interact with each other producing complex microphysics. Field
79 campaigns using high spatiotemporal resolution airborne radars (e.g., ProfiLing Of Winter Storms
80 [PLOWS], e.g. Rauber et al. 2014) revealed microscale convective updrafts producing generating
81 cells, which contributed to greater ice production by vapor diffusion, riming, and aggregation
82 processes (Plummer et al. 2014). Kumjian and Lombardo (2017) observed planar crystal growth
83 and precipitation-type transitions (snow/rain/ice) in snowbands using the dual-polarization
84 capabilities from the WSR-88D radar network. They also found a signature of secondary ice
85 production. Those detailed, complex microphysical evolution in winter storms might not be
86 captured by regional models (e.g., the Rapid Refresh model reanalysis with 50 vertical levels and
87 13-km horizontal grid spacing, Kumjian and Lombardo 2017) and even by cloud resolving models,
88 likely due to deficiencies in many of the bulk microphysical schemes for winter storms (e.g.,
89 Naeger et al. 2017;2020; Molthan et al. 2016). Motivated by those gaps in understanding
90 microphysics and less representativeness in numerical models, the field campaign, the
91 Investigation of Microphysics and Precipitation of Atlantic Coast-Threatening Snowstorms
92 (IMPACTS, McMurdie et al. 2022) focuses on improving the understanding of snowfall processes,
93 remote sensing of snow, and the prediction and evolution of banded structures. The campaign
94 achieved multi-scale observations including in-situ and vertically-pointing and scanning remote
95 sensing measurements from both airborne and ground-based platforms.

96 Previous observational studies (e.g., Plummer et al. 2015; Rauber et al. 2014; Rauber et al.
97 2017) corroborated the importance of turbulence to generate ice particles and intensify snowfall.
98 Turbulence often has been observed by fine-scale Doppler radar observations to occur in multiple
99 layers within stratiform snow clouds with frequent periodic upward/downward patterns within
100 stratiform precipitation clouds without terrain forcings (e.g., Rauber et al. 2017). The upward
101 motions could contribute to supply water vapor and hence further ice formation and/or growth
102 resulting in generating cells (Kumjian et al. 2014) and intensifications of snow fallstreaks
103 (Plummer et al. 2015; Rauber et al. 2017), as shown by prominent radar reflectivity compared to
104 the background. One of the common factors that generate instability and turbulence in stratiform
105 clouds is wind shear (i.e. Kelvin–Helmholtz instability). Previous studies such as Boucher et al.
106 (1965), Wexler et al. (1967), and Syrett et al. (1995) observed wind shear varying in time in winter

4

storms using Doppler radar measurements and suggested that the wind shear could play a role in the formation of generating cells. Rauber et al. (2014) revealed multiple sources of air masses with different wind directions and humidity associated with a comma head snowstorm. The multi air masses controlled cloud structure including cloud depth, instability, and vertical wind shear and produced cloud-top turbulence and generating cells. Despite the importance of generating cells, as well as turbulence that contributes to vertical air motion, for snowfall intensification, the formation process of the turbulent layers and the roles in snowfall formations are still unclear. Such turbulence structures are usually not resolved by either regional models or operational radars.

In this study, we hypothesize that 1) this upward motion associated with fine-scale turbulence contributes to snowband formation and 2) the turbulence producing the updrafts is generated by wind shear and/or thermodynamic instability in association with Kelvin–Helmholtz instability. Particularly we investigate i) frequency of upward motion component of fine-scale turbulence during the individual storms, ii) contribution of the updrafts to the upward mass transport, iii) relationships amongst the fine-scale upward motion, wind shear, and thermodynamic stability, and mesoscale forcing for ascent (e.g. frontogenesis).

The Ka-band Scanning Polarimetric Radar (KASPR) is an ideal remote sensing instrument to study the fine scale kinematic and microphysical characteristics of winter storms (e.g. Oue et al. 2017; Kollias et al. 2020). KASPR has been part of the Stony Brook University and Brookhaven National Laboratory Radar Observatory (SBRO) since 2017 and is installed at the Stony Brook University site (Fig. 1). KASPR polarimetric and Doppler capabilities have revealed fine scale dynamical and microphysical features within winter storms (Kumjian et al. 2020; Lamer et al. 2021; Oue et al. 2021).

This study uses data from four winter storms and focuses on characteristics of microscale (< 1 km) updraft regions, their relationship with ambient conditions, and their role in vertical mass transport. Section 2 describes the datasets used in this study. Section 3 summarizes the meteorological context and evolution of the four events and the corresponding KASPR observations. The relationships among the observed updraft structures, precipitation features, and other storm parameters important for forcing for ascent (e.g., frontogenesis, Petterssen, 1956) and wind shear are discussed in section 4. Finally, summary and conclusions are presented in Section 5.
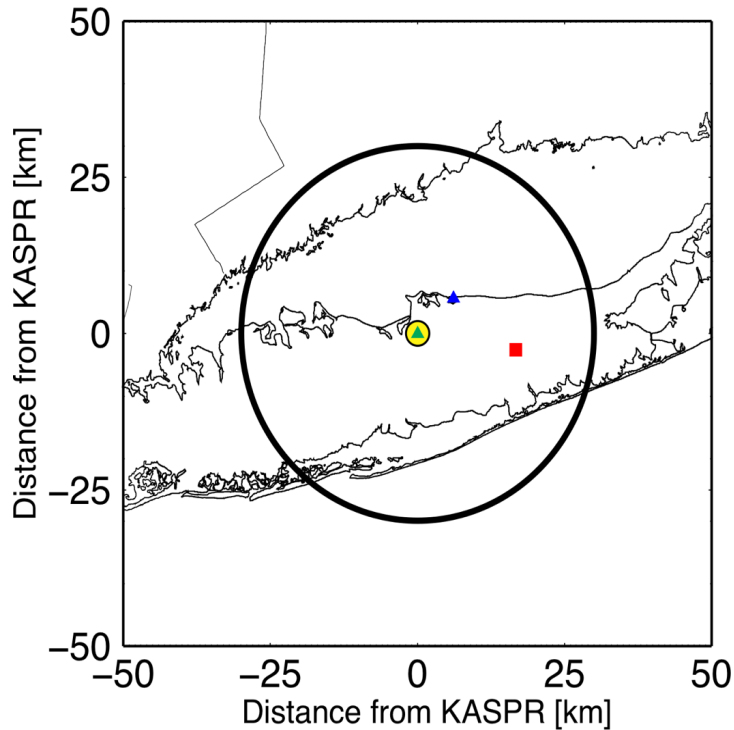
Figure 1: Locations of KASPR (the center of this display, yellow dot), the nearest NWS sounding site (OKX, red square), and two SBU mobile sounding sites (SBU by green triangle and Cedar Beach by blue triangle). A large circle represents the KASPR's 30-km radius maximum observation range.

2. Data and Methods

a. *Ka-band Scanning Polarimetric Radar (KASPR)*

KASPR is a state-of-the-art 35-GHz cloud scanning radar with a beamwidth of 0.32°, capable of collecting reflectivity, Doppler velocity, Doppler spectrum width, and the standard set of polarimetric radar variables. The KASPR power measurements are calibrated using a corner reflector technique. The detailed specification of KASPR is available in Kumjian et al. (2020) and Kollias et al. (2020).

During winter storm observations, KASPR executed a scanning strategy that consisted of a Plan Position Indicator (PPI) surveillance scan at 15° elevation angle (and 20° for the 2018 winter), a zenith pointing (90° elevation angle) PPI for calibration, horizon-to-horizon Range-Height Indicator (RHI, Kollias et al., 2014) scans, and a vertically pointing mode (VPT). Following Kumjian et al. (2020), this pattern was repeated and took approximately 13-15 minutes to complete, providing the slant PPI surveillance scans every 7 minutes (15 minutes for the 2018 winter). RHI scans crossing and/or along the snowbands were performed in each cycle producing

160   RHI scans toward the same direction every 40 seconds to 3.5 minutes (40 seconds to 15 minutes

161   for the 2018 winter). The PPI and RHI scans were performed with a full polarimetry mode and

162   scan speeds of 6° s^{-1} and 2° s^{-1}, respectively, to collect data with a 30-m range-gate spacing, 0.6°

163   PPI azimuthal spacing and 0.3° RHI elevation spacing. The VPT mode was executed with only

164   horizontally polarized waves transmitted and both horizontally and vertically polarized waves

165   received. The KASPR radar was in VPT mode for consecutive periods lasting 2 to 5 min with a

166   15-m range-gate spacing. Based on the beamwidth, the horizontal resolution at a 10 km range is

167   approximately 56 m. This study did not apply attenuation corrections for hydrometeors, and

168   carefully selected periods when ice precipitation dominates through the cloud to avoid significant

169   attenuation by liquid precipitation. If the column included liquid precipitation signatures, which

170   could be defined by the presence of melting layer(s) in the VPT measurements, the column is

171   excluded from the analysis.
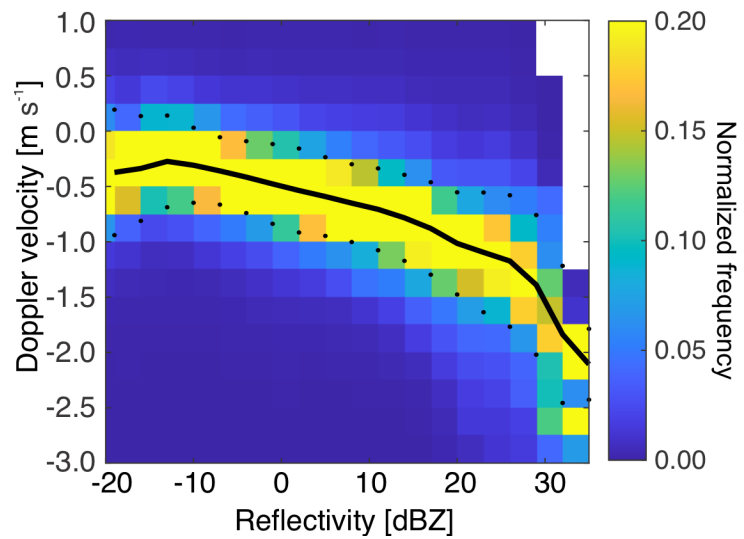
172
173   Figure 2: Reflectivity versus mean Doppler velocity from all KASPR VPT data used in this study from the
174   selected four cases. Color shade represents frequency normalized every 3 dB. Solid and dotted lines represent
175   mean Doppler velocity every 3 dB and mean Doppler velocity ± standard deviation, respectively. Negative
176   Doppler velocity values indicate downward motion. Doppler velocity is scaled for air density using the nearest
177   sounding data.
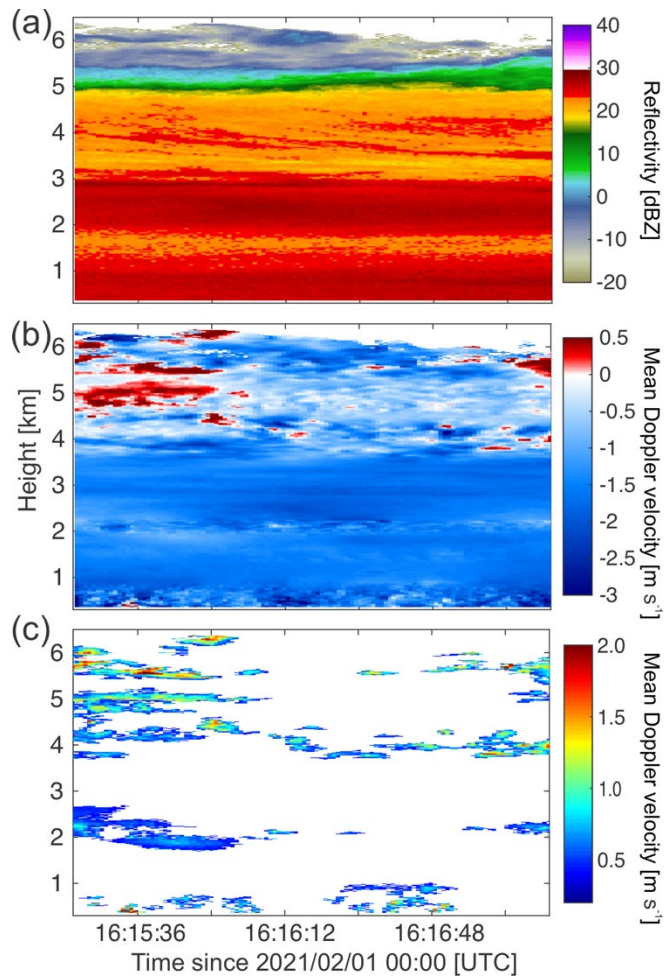
Figure 3. Height-versus-time cross sections of (a) KASPR reflectivity and (b) mean Doppler velocity from vertically-pointing measurements on February 1, 2021 from 16:15:18 to 16:20:10 UTC, (c) the estimated upward vertical air motion > 0.4 m s^{-1} (estimated after removing hydrometeor fall speed from the measured Doppler velocity). Very small updraft regions < 15 range-bins are not included in the analysis.

The VPT measurements were used to identify updraft regions (URs) in time-height plots based on mean Doppler velocity. First, Doppler velocity with reflectivity < -20 dBZ was removed from the analysis since it was too noisy. Then the hydrometeor sedimentation component (i.e. fall speed) was removed from the measured Doppler velocity following Protat and Williams (2011) using reflectivity versus Doppler velocity (Z-V) relationships. In this study, the hydrometeor fall speed was estimated as the median Doppler velocity for every 3 dB from -20 dBZ to 34 dBZ, assuming that the mean vertical air motion for a certain time period at a given height was ~0 m s^{-1}. Whenever >100 samples were available in a bin and median Doppler velocity was negative, we estimated the Z-V relationship every 500 m using hourly VPT data and used the median value of Doppler velocity as the hydrometeor fall speed at each Z bin at each height-hour window. For bins with few

194 observations (<100 samples) or a positive median Doppler velocity (ascent), we instead used the

195 statistical value of the median Doppler velocity estimated from all VPT data shown in Fig. 2 (black

196 line) as the hydrometeor fall-speed estimate. To avoid accounting for range gates not representing

197 updrafts due to the variability of the Doppler velocity, we considered updraft regions to be range

198 gates where the measured Doppler velocity minus the estimated hydrometeor fall speed was

199 greater than equal to 0.4 m s^{-1}. The threshold of 0.4 m s^{-1} is the value of standard deviation of

200 Doppler velocity in Fig. 2. For example, in Fig. 2, for -1 dBZ the estimated fall speed is -0.48 m

201 s^{-1} so measured Doppler velocity values > -0.08 m s^{-1} are considered to be updrafts. For 20 dBZ

202 the estimated fall speed is -1.01 m s^{-1} so measured Doppler velocity values > -0.61 m s^{-1} are

203 considered updrafts. We defined the updraft region (UR) as a region with at least 15 updraft range-

204 gates connected in time or height. Small regions having less than 15 range-bins are removed from

205 the analysis.

206 Figure 3 shows an example of 5-min VPT reflectivity (Fig. 3a), Doppler velocity (Fig. 3b), and

207 the identified updrafts from 16:15:18 UTC for 5 minutes on 1 February 2021. We tested other

208 Doppler velocity thresholds (0.0 m s^{-1} and 0.6 m s^{-1}) that were applied to the Doppler velocity after

209 the sedimentation (i.e. fall speed) removal and confirmed that varying the threshold within this

210 range had little impact on the results. For example, when the threshold is increased from 0.4 m s^{-1}

211 to 0.6 m s^{-1}, the total number of URs decreases by 28-49%; however, the shapes of the normalized

212 size distribution (discussed in Section 4) and vertical distribution do not change. Because of the

213 uncertainty of the detected numbers of URs that depend on the thresholds, the analysis in this study

214 focuses on qualitative descriptions rather than quantitative discussion.

215 The duration of the detected URs is the time between the earliest and latest times of the

216 appearance of the UR region. The vertical extent is the height between the lowest and highest

217 range-bins of the appearance of the region. The altitude of individual updraft regions is estimated

218 as a mean of altitudes of range gates in the updraft regions (Fig. 3c). Fine scale turbulence can

219 contribute to Doppler spectrum width (SW, Appendix A). For the VPT measurements using the

220 narrow beamwidth (0.3°) in this study, the wind shear component in the observed SW would be

221 mostly dominated by horizontal/vertical gradients in vertical air motion within the radar range

222 gate. We use SW > 0.4 m s^{-1} from the VPT measurements to represent the fine-scale turbulence

223 (Appendix A). The Doppler spectrum width (SW) from the VPT measurements is averaged in each

224 UR.

225   To understand the role of URs on snowfall intensification, we estimate the upward mass flux

226   based on the detected URs. The bulk mass flux (MF) at each altitude can be estimated as:

227    $$MF = \overline{W} \rho_d UF \quad [\text{kg m}^{-2} \text{ s}^{-1}] \tag{1}$$

228   where $\overline{W}$ is the mean updraft that is the positive Doppler velocity from the detected updraft regions

229   averaged over time at each altitude, ρ_d is the dry air density estimated from the nearest-time

230   sounding measurements, and UF is the updraft fraction estimated as the ratio of the time of updraft

231   (positive Doppler velocity in the detected updraft regions) to the total cloudy time for each VPT

232   file (bulk mass flux). The mass flux profile from each VPT file is then averaged > 1.2 km above

233   ground level (AGL) for each VPT file (column mean mass flux).

234   Because we highlight the importance of shear-driven turbulence, we compute vertical wind

235   shear, which measures the likelihood of turbulence. The Kelvin–Helmholtz instability can appear

236   when the Richardson Number is small ($< \sim 0.25$). Here we introduce the moist Richardson Number

237   (mRi) to represent the instability in this cloudy environment. First, we estimate wind direction and

238   speed from KASPR PPI measurements at an elevation angle of 15° (approximately every 7

239   minutes) using a velocity-azimuth display (VAD) technique (Browning and Wexler, 1968). Using

240   the VAD data up to maximum height of 7.8 km AGL, we estimated the vertical wind shear

241   (V_{shear}):

242    $$V_{shear} = \sqrt{\left(u_{z_2} - u_{z_1}\right)^2 + \left(v_{z_2} - v_{z_1}\right)^2} / (z_2 - z_1) \tag{2}$$

243   where z represents height and u_z and v_z represent horizontal wind components at z. We use a 100

244   m (124 m for the January 4 case) spacing to estimate V_{shear} at each VAD data point ($z_2 - z_1 = 100$

245   m). Since only a single elevation angle is used for the VAD, the resulting horizontal wind profile

246   is based on an increasing diameter cone with increasing height (~ 7.5 km diameter for 1 km altitude

247   and ~ 59.7 km for 8 km altitude). The moist Richardson Number (mRi) is calculated using the

248   following equation (Markowski and Richardson, 2010):

249    $$mR_i = \frac{N_m^2}{\left(\frac{\Delta u}{\Delta z}\right)^2 + \left(\frac{\Delta v}{\Delta z}\right)^2} \tag{3}$$

250   N_m is the Brunt–Väisälä frequency defined as:

251    $$N_m = \sqrt{\frac{g}{\theta_e} \frac{\Gamma_m}{\Gamma_d} \frac{\Delta \theta_e}{\Delta z}} \tag{4}$$

252

253 where θ_e is equivalent potential temperature, Γ_d and Γ_m are dry adiabatic lapse rate and pseudo

254 adiabatic lapse rate, respectively, and g is Earth's gravity. θ_e and Γ_m were estimated from the

255 nearest soundings. u and v are horizontal wind components, which can be obtained from soundings

256 or the KASPR VAD measurements. A $\Delta z=100$ m (124 m for the January 4 case) was used in this

257 study. Γ_m was estimated using the following equation (Markowski and Richardson, 2010):

258
$$\Gamma_m = \frac{g + \frac{dL_v r_v}{dz}}{c_{pd} + r_v c_l} \qquad (5)$$

259 where L_v is the latent heat of vaporization, r_v is the water vapor mixing ratio, c_{pd} is the specific

260 heat of dry air at constant pressure, and c_l is the specific heat capacity of liquid water.

261

262 *b. Sounding and WSR-88D radar data*

263   Twice-daily radiosonde data at 0000 and 1200 UTC were used from the nearest NWS site

264 (OKX; red square in Fig.1), which is ~22 km to the east of Stony Brook. For the events in 2020

265 and 2021 additional soundings were launched every ~3 hours using the GRAW sounding system

266 installed on a Stony Brook University (SBU) mobile radar truck. The SBU mobile radar truck was

267 deployed in several locations in Long Island including Cedar Beach (40.965N, -73.030E; blue

268 triangle in Fig. 1; for 18 January 2020) and Stony Brook University (40.897N, -73.127E; green

269 triangle in Fig. 1; for 17 December 2020 and 1 February 2021).

270   To provide the regional precipitation context for these snow events, we used the radar

271 reflectivity from the NEXRAD WSR-88D surveillance scans at the lowest two elevation angles

272 (i.e., 0.5 and 0.8º) at the KOKX site.

273

274 *c. Reanalysis data*

275   The Rapid Refresh reanalysis (RAP; Benjamin et al. 2016) was used to examine the

276 environment and frontogenesis during the snowstorm events. It uses hourly-updated data

277 assimilation with 37 pressure levels and 13.5-km grid spacing.

278   The mean sea level pressure from the fifth generation of the European Centre for Medium-

279 Range Weather Forecasts (ERA5; Hersbach et al. 2020) was used to track cyclone centers. It

280 provides hourly data interpolated into 37 pressure levels at 0.25° grid spacing. The cyclone

281 tracking was based on the mean sea level pressure value less than 1010 hPa, gradients of the mean

282   sea level pressure, and the distance from the previous cyclone center, following Crawford et al.

283   (2021).

284

285   *d. Snow events*

286   We examined four snowstorm cases: 4 January 2018; 18 January 2020; 16 – 17 December

287   2020; and 31 January to 1 February 2021. Three cases (4 January 2018; 16 – 17 December 2020;

288   and 31 January to 1 February 2021) had multibands, while the other case (18 January 2020)

289   included a primary band (Table 1). The track of the surface low pressure centers for the storms are

290   shown in Fig. 4. The cases were chosen to provide a diverse set of band structures within the

291   cyclone comma head. Table 1 summarizes the storm characteristics and sample size for each case.

292   Brief descriptions of the cases and synoptic conditions will be shown in Section 3b.

293

	Storm Quadrant	Types of bands within storm	Trend in storm Z intensity as it passed over Stony Brook (based on NEXRAD)	Period	Total cloudy time analyzed by VPT [min]	No. of VPT files used	No. of VAD profiles (PPI data files) used	Sounding time (day/hour) [UTC]
4 Jan 2018	S	Multibands	Sustain Z >30 dBZ	10:09 – 23:55 UTC	278.2	56	138	04/12, 05/00
18 Jan 2020	NW~W	Single-band	Weaken from 30 dBZ to < 25 dBZ.	14:10 – 23:59 UTC	196.7	80	80	18/12, 18/18, 18/19, 18/21, 19/00
16 – 17 Dec 2020	N~NW	Multibands	Sustain Z >30 dBZ	18:22 UTC on Dec. 16 – 02:59 UTC on Dec. 17	184.1	75	76	16/12, 17/00, 17/03
31 Jan –1 Feb 2021	N	Multibands	Weakening from 40 dBZ to 30 dBZ.	18:02 UTC on Jan. 31 – 23:51 UTC on Feb. 1	236.4	119	170	31/12, 01/00, 01/06, 01/08, 01/12, 01/15, 01/18, 01/21, 02/00

294
295   Table 1. Summary of the storm characteristics and sample sizes. Soundings at 00 and 12 UTC are from the

296   NWS OKX soundings, and the others are from the SB mobile truck.
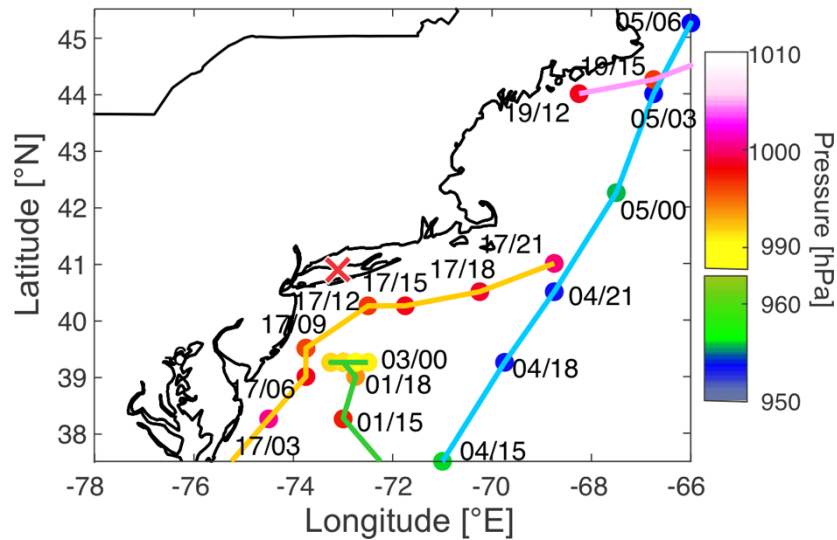
Figure 4: Tracks of the cyclone centers every three hours using ERA5 mean sea level pressure for the cases of 4 Jan 2018 (blue line), 18 Jan 2020 (magenta line), 17 – 16 Dec 2020 (orange line), and 31 Jan–1 Feb 2021 (green line). Color for each dot represents the surface central pressure (in hPa) every three hours. Cross mark represents the Stony Brook location.

3. Results

a. Characteristics of detected updraft regions

Table 2 lists the number of the URs detected within the cloud echo observed by the KASPR VPT measurements, and those normalized by the total cloudy time per 5 minutes (number per 5 min), which is defined as an accumulated time where KASPR observed cloud echoes at any altitude during the analysis period. The warm frontal band case on 18 January 2020 has the lowest number of the updraft regions per 5 min among the four cases (~10 per 5 min). The other cases have 2-5 times more URs.

We identified the URs below ~1.2 km AGL for all cases. These are likely associated with the boundary layer turbulence. To focus on updrafts that may have strong relationships with storm evolution, wind shear, and shear-induced turbulence in clouds, we do not include the boundary layer updraft regions in the present analysis. The height of the planetary boundary layer (PBL) was determined as the bottom of the temperature inversion layer near the surface using the sounding

profiles. They are 0.5 km for 4 January, 0.9 km for 18 January, 1.1 km for 16-17 December, and 0.7 km for 1 February 2021. The numbers of URs above the PBL are also listed in Table 2.

	Total number	Above PBL	Average Per 5 min	Normalized number per 5 min above PBL	Number with SW > 0.4 m s^{-1} for height above PBL
Jan 4, 2018	3376	2923 (86.6%)	60.7	52.5	1142 (39.1%)
Jan 18, 2020	673	517 (76.8%)	17.2	13.2	21 (4.1%)
Dec 16 – 17, 2020	2774	2311 (83.3%)	75.3	62.8	667 (29.9%)
Jan 31 – Feb 1, 2021	2171	1728 (79.6%)	45.9	36.5	542 (31.4%)

Table 2. The number of detected updraft regions in total and normalized per 5 minutes (number per 5 min). The numbers of detected updraft regions counted for heights above the planetary boundary layer (PBL) are also listed. The percentages in the parenthesis in the right most column represents those of the total number of URs for height above the PBL.

Figure 5a shows frequency distributions of the duration of URs detected above the PBL within a 10-sec interval. Even though the number of detected URs varies by event, the qualitative characteristics of the duration time distribution is similar for all four cases. There is a peak at the smallest size bin for the four cases, and overall, the number exponentially decreases with size. Most of the updraft regions last for less than 20 sec (i.e., small size in the height-time plots), accounting for approximately 80% of the total. The maximum duration bin is 95 sec. This distribution shape and qualitative features do not change when different thresholds are used for mean Doppler velocity (Sect. 2a). The distribution curves from the three cases that had more than 1700 updraft regions show similar exponential distribution. Considering that the horizontal extent of UR can be roughly estimated as duration × horizontal wind speed estimated from the KASPR VAD, approximately 85% of URs have the horizontal scale < 500 m. It is highly possible that portions of the URs passed through the radar site rather than the part of the maximum dimensions and the horizontal scale could be an underestimate. Although it is difficult to estimate URs using the tilted scans, the KASPR RHI measurements showed cell-like features with horizontal scale < 500 m. The mean vertical extent of URs from the VPT measurements is 261 m for all cases, and more than 81% of URs have vertical extents less than 330 m. The aspect ratio of the URs (defined

345   as the ratio of the horizontal scale to the vertical extent) for each case shown in Fig. 5b has a

346   lognormal frequency distribution with the frequency peak around 1 (i.e., circular).
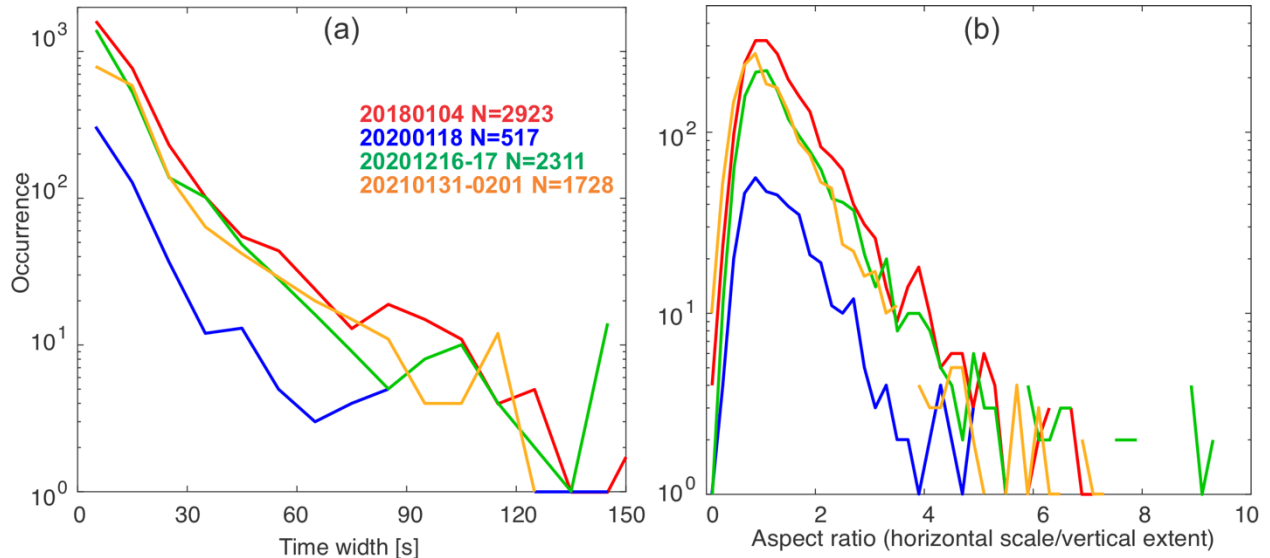
347
348   Figure 5: Distributions of (a) time-width of the URs with the time bin size of 10 s for 4 Jan 2018 (red), 18 Jan
349   2020 (blue), 16 – 17 Dec 2020 (green), and 31 Jan – 1 Feb 2021 (orange) and (b) aspect ratio of the URs
350   defined as the ratio of horizontal scale to the vertical extent with the aspect ratio bin size of 0.2. The time width
351   for each updraft region is defined as the time between the time when the updraft region appeared first and the
352   time when it disappeared. The horizontal scale is estimated using the time width and the horizontal wind speed
353   estimated from the KASPR VAD measurements. The sample size for each case is shown in the right corner in
354   (a).

355

356

357   Table 3 summarizes the characteristics of the detected URs for each case. The URs have a

358   median vertical extent of 150 – 240 m. We classified the regions for smaller and larger SW from

359   the KASPR VPT measurements with a threshold of 0.4 m s^{-1}; UR with SW < 0.4 m s^{-1} named

360   URSWLO and UR with SW > 0.4 m s^{-1} named URSWHI. Higher values of SW > 0.4 m s^{-1} can be

361   a proxy for higher magnitudes of turbulence (Appendix A). The URSWHIs are thicker than

362   URSWLOs for all cases, but the difference varies between 0 m (16 – 17 December) and 90 m (18

363   January). Considering the range-gate spacing for the VPT measurements, the difference in the

364   number of range-gates for the vertical extent is less than 6. These qualitative characteristics do not

365   change significantly when the Doppler velocity threshold for the detection is changed to 0.2 and

366   0.6 m s^{-1}.

367

368

	Median duration (sec)		Median vertical extent (m)		Median maximum upward motion (m s^{-1})		Median reflectivity (dBZ)	
	URSWHI	URSWLO	URSWHI	URSWLO	URSWHI	URSWLO	URSWHI	URSWLO
4 Jan 2018	7.2	9.3	180	150	1.26	0.74	16.64	8.36
18 Jan 2020	6.2	8.3	165	150	1.15	0.78	19.95	5.78
16 – 17 Dec 2020	7.2	8.3	180	180	1.08	0.88	13.00	-3.36
31 Jan – 1 Feb 2021	9.3	11.4	165	135	1.29	0.77	7.77	4.32
All cases	7.2	9.3	165	150	1.18	0.79	14.45	4.24

Table 3. Median duration, vertical extent, maximum upward motion (maximum Doppler velocity without estimated fall speed in each UR), and reflectivity from the KASPR VPT moments for UR with SW>0.4 m s^{-1} (URSWHI) and SW<0.4 m s^{-1} (URSWLO) found at heights > 1.2 km.

b. Spatial distributions of updraft regions

1). 4 January 2018

At 1200 UTC 4 January 2018, a deep surface cyclone (~968 hPa) was located a few hundred kilometers to the southeast of Long Island, NY. As the storm center moved from south of Long Island to the northeast (blue track in Fig. 4), the snowbands within the comma head produced heavy snow across Long Island from 1000 UTC 4 January to 0100 UTC 5 January 2018. Figure 6 shows the horizontal distributions of the NEXRAD reflectivity at the time of snowbands, 700 hPa RAP, and the 1200 UTC sounding profile. From 0900-1730 UTC, narrow snowbands (to 25 dBZ) orientated north-northeast to south-southwest crossed SBU (Fig. 6a), about 300 km northwest of the surface cyclone (Fig. 4). The snowband pivoted and changed its motion from westward to eastward around 1730 UTC, as the cyclone center moved ~500 km southeast of Long Island. The snowbands passed over SBU from west to east around 2030-2100 UTC. After the passage of the snowband, several relatively weak reflectivity bands < 25 dBZ, oriented along north-to-south or north-northwest-to-south-southeast passed through SBU until 0200 UTC on 5 January 2018. At 700 hPa (Fig. 6b), southeasterly wind with the closed low resulted in warm advection extending northward to Long Island, likely producing vertical wind shear.

The NWS sounding at 1200 UTC on 4 January shows a gradual wind veering from northeasterly below 2.5 km above mean sea level (ASL) to southerly at 6-km ASL (Fig. 6c), while there was a stable layer with a shallow frontal zone from 0.4-0.8 km ASL. From Eq. 1, there were relatively

large vertical wind shear layers (> 15 m s^{-1} km^{-1}) below 6 km ASL (e.g., 0.8, 1.3, 1.9, 3.5, 4.6, and 5.7 km, Fig. 5c). They generally corresponded to heights of positive gradient of temperature (black line) and θ_e (blue solid line), and a few of them corresponded to the mRi < 0.25 (indicated by gray shades in Fig. 6c).
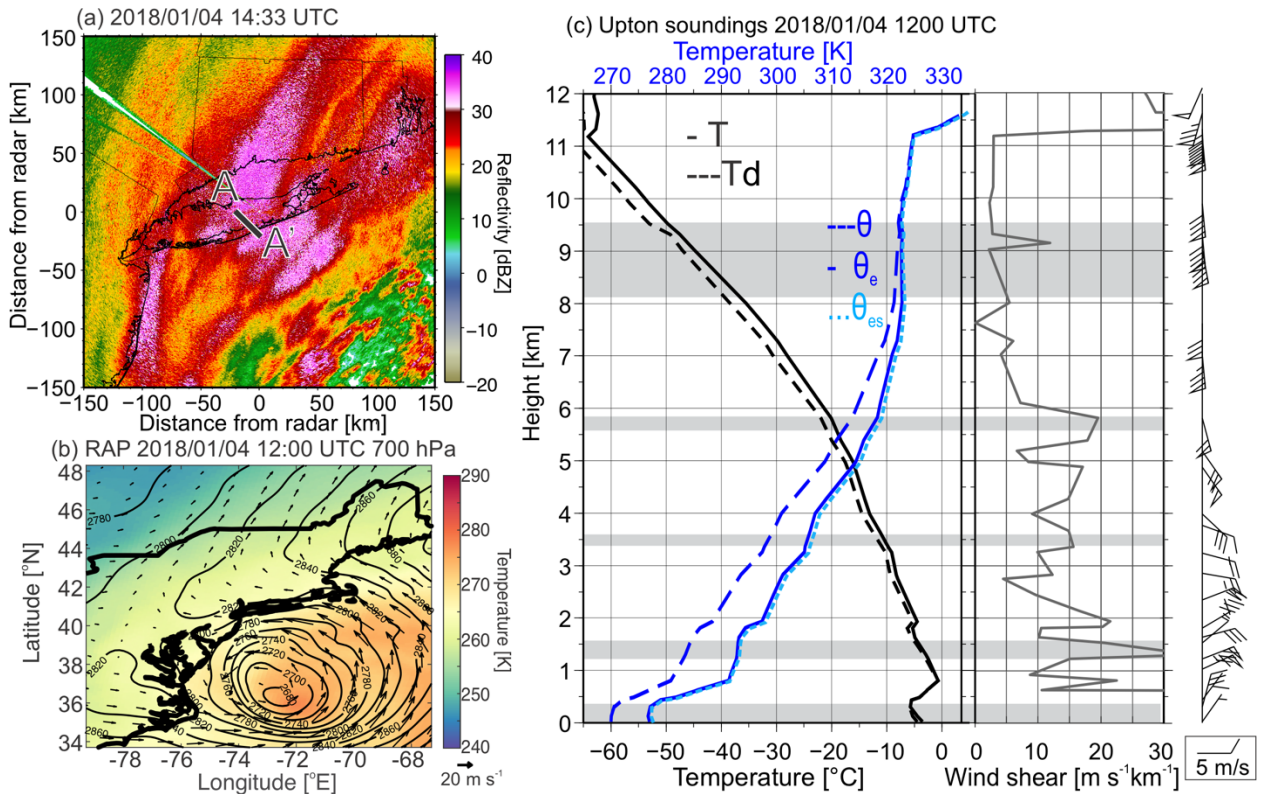
Figure 6: (a) Horizontal distribution of KOKX reflectivity from a PPI scan at an elevation angle of 0.5° at 1433 UTC on 4 Jan 2018, (b) 700-hPa temperature (color shade), geopotential height (contour) and horizontal wind (arrows) from RAP reanalysis data at 12 UTC on 4 Jan 2018. (c) Sounding profiles of temperature (black solid line), dew point temperature (black dashed line), potential temperature (θ blue dashed line), equivalent potential temperature (θ_e blue solid line), saturated equivalent potential temperature (θ_{es} light blue dashed line), and vertical wind shear estimated from Eq. 1 (gray line in the right panel) at 1200 UTC from OKX. Gray shaded layers in (c) represent layers of moist Richardson Number (mRi) < 0.25. The A – A' line in (a) represents the KASPR RHI direction shown in Fig. 7a-c.

Figure 7 shows vertical cross sections of the snowbands from the KASPR RHI and height-versus-time plots during the snowband from the VPT measurements. The KASPR RHI measurements across the snowbands at 1432 UTC (135° in azimuth, Fig. 7a-c) reveal individual cells between 4-7 km altitudes and fallstreaks underneath. The KASPR reflectivity and Doppler velocity from the VPT measurements (Fig. 7d,e) also reveal updrafts in the convective cell layer and the fallstreaks attaining the 30-dBZ reflectivity. This convective cell layer at 4-7 km is collocated with a relatively large SW of approximately 0.4 m s^{-1} in VPT (Fig. 7f). The SW layers

presented in the VPT measurements are consistent with the vertical wind shear shown at 5-6 km

ASL in the RHI Doppler velocity A-A' (Fig. 7b) and sounding profile (Fig. 6c). They suggest a

role of turbulence in forming convection and intensifying snow.
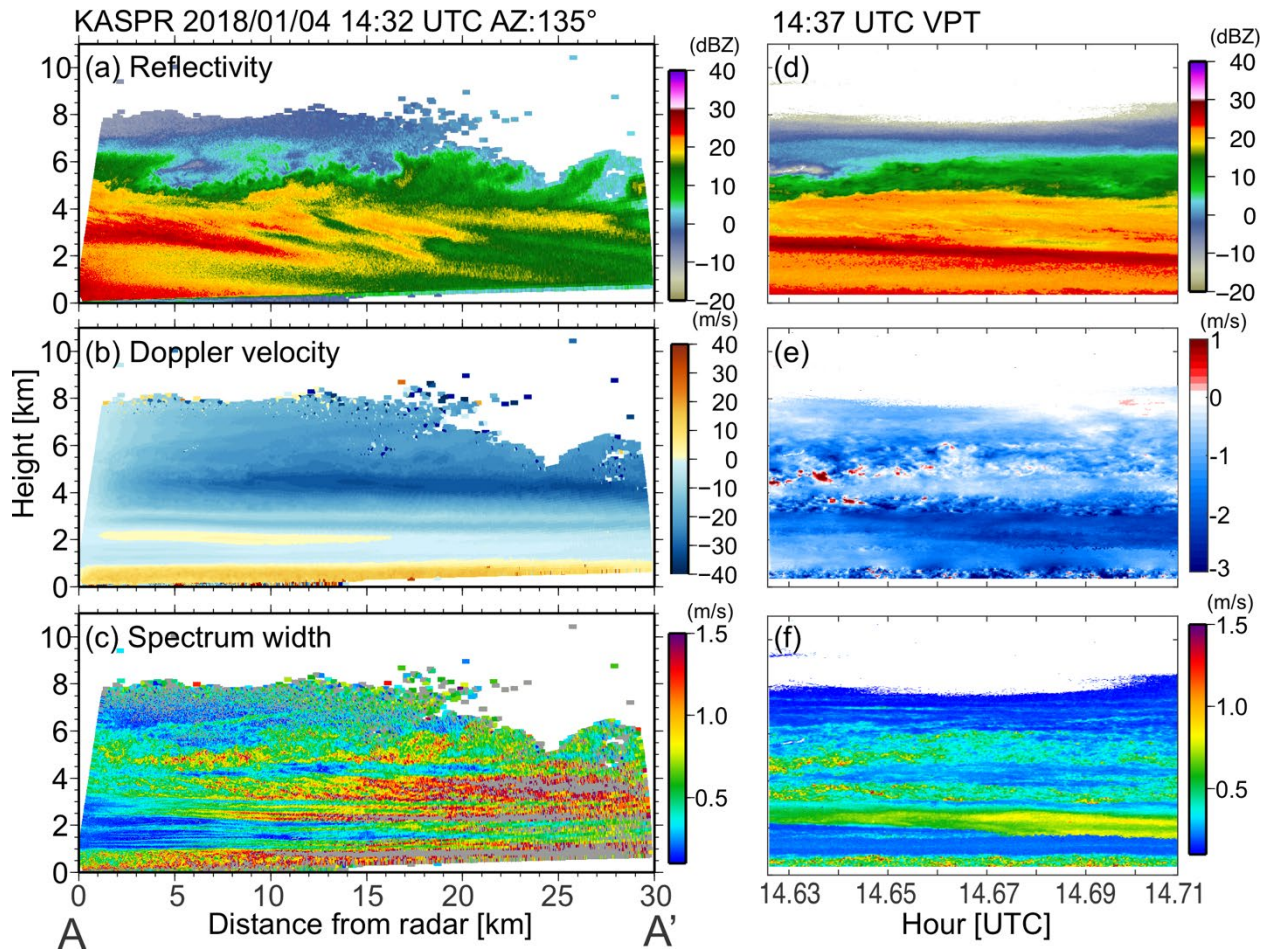
Figure 7: Vertical cross sections of KASPR (a) reflectivity (shaded in dBZ), (b) mean Doppler velocity in m s^{-1}, (c) Doppler spectrum width in m s^{-1} from an RHI scan along A-A' line in Fig.6a at 1432 UTC, and height-versus-cross sections of KASPR (d) reflectivity, (e) mean Doppler velocity, (f) Doppler spectrum width from the VPT measurements.

To investigate the spatial characteristics of URs associated with wind shear, we show locations

of the detected updraft regions (dots) in the height-time cross section fields for individual cases in

Fig. 8a, with color shade representing SW from the KASPR VPT measurements and grayscale

representing KASPR reflectivity from VPT. We also show wind directions (color shade) and

vertical wind shear (contours) from the KASPR VAD analysis in Fig. 8b. To examine a relation

with a large scale forcing, we also show the time series of frontogenesis at 600, 700, 775, and 800

430   hPa (Bluestein, 1993) using RAP reanalysis data in Fig. 8c. The mRi < 0.25 calculated from

431   sounding and KASPR VAD data is shown in Fig. 8d by magenta contours.

432
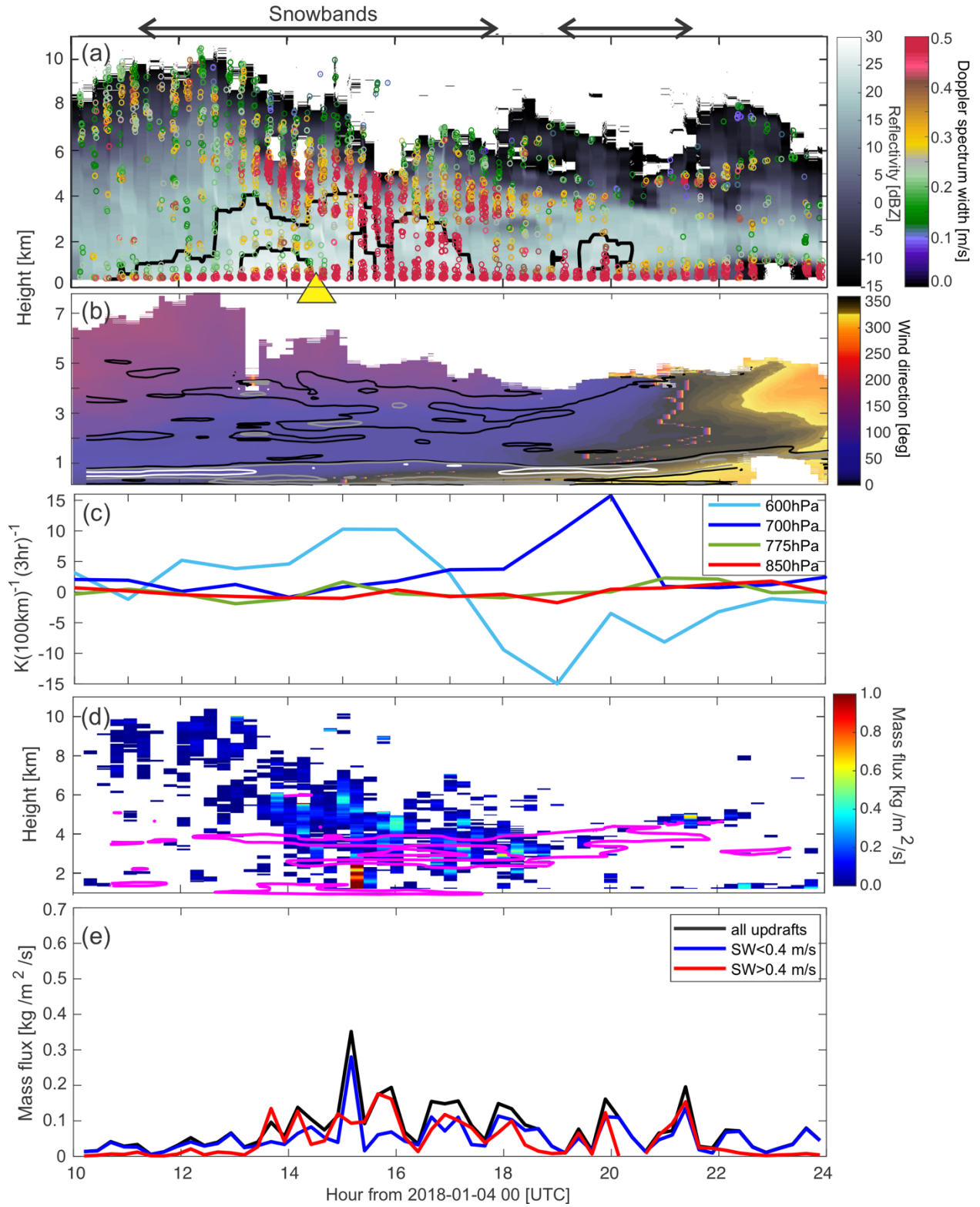
Figure 8: (a) Height-versus-time cross sections of KASPR reflectivity from VPT (gray scale) and locations of detected updraft regions (color dots) for 4 January 2018. Black contours represent KASPR reflectivity >20 dBZ with 5 dB increment. Horizontal arrows on the top represent the period of snowband passages at SBU. Yellow triangle indicates the time of the snowbands near SBU shown in Fig. 4 and RHI measurements shown in Fig. 7. (b) Height-versus-time cross sections of wind direction (color shade) and vertical wind shear of 0.02, 0.03, and 0.05 s^{-1} (black, gray, and white contours, respectively) estimated from KASPR VAD. (c) Time series of frontogenesis at four levels at four levels estimated using RAP reanalysis data for 4 January 2018. (d) Height-versus-time cross sections of the bulk mass flux (color shade) and mRi smaller than 0.25 (magenta contour). The mass flux is averaged every VPT file at each height. (e) Time series of column mean mass flux estimated from the detected updraft regions averaged over altitude. The mass flux is averaged every VPT file and then averaged over altitude. Black line represents the column mean mass flux from the contributions of all detected updraft regions, and blue and red lines represent that of updraft regions with SW>0.4 m s^{-1} and <0.4 m s^{-1}, respectively.

URs are more frequently observed during the first snowband period (1110–1800 UTC), suggesting a contribution of URs to the snowbands, as shown in the previous studies. The URs are also observed outside the snowbands. A difference between the URs during the first snowband and those outside the first snowband period is that the URs during the first more accompanied URSWHIs above 2 km ASL (Fig. 8a, represented by brown-red dots). The URSWHIs appear in the mid-level of the cloud, consistent with the earlier snowband period producing reflectivity >20 dBZ below 4 km altitude, which is 5-dB stronger than that of the latter snowband (Fig. 8a). The URSWHI height is 6 km at 1300 UTC and then descends to 3.5-4 km at 1800 UTC (Fig. 8a). URSWLOs (represented by yellow-green dots) are found at 2-km below the cloud top before the snowband period from 1000 UTC through the entire period of precipitation until 0000 UTC on 5th. From the KASPR VAD (Fig. 8b), the period (1300 - 1800 UTC) when URSWHIs dominate the mid-levels corresponds to the easterly wind associated with the cyclone below 5 km. This low-level wind produces a vertical wind shear with the upper-level southerly wind shown in the sounding (Fig. 6c). The low-level easterly flow corresponds to the veering wind around the storm center accompanying a warm air shown at 700 hPa. The URSWHIs are also collocated with vertical wind shear > 20 m s^{-1} km^{-1} in the KASPR VAD (Fig. 8b, black contour). This is consistent with the low mRi < 0.25 (Fig. 8d, contour) suggesting shear instability. The number of the URs decreases after 1830 UTC close to the end of the first snowband passage and the frontal passage. The low mRi is still present at 4 km altitude, but the wind direction changes to north to northwesterly. The earlier snowband period (1110–1800 UTC) is well associated with 600-hPa frontogenesis, with a peak exceeding 10 K $(100 \text{ km})^{-1}$ $(3hr)^{-1}$ (Fig. 8c, light blue), while there is 700-hPa frontogenesis exceeding 15 K $(100 \text{ km})^{-1}$ $(3hr)^{-1}$ for the latter snowband (1900 – 2110 UTC) (Fig. 8c, blue).

469   The height-time cross sections of bulk mass flux and the time series of column mean mass flux
470   are displayed in the time series plots in Figs. 8d and 8e, respectively. Figure 8d also show the mRi
471   less than 0.25. Generally, the URs contributed to upward bulk mass flux when they are clustered
472   in space and time. The URs during the snowbands above 2 km contributed relatively large mass
473   flux (Fig. 8d), and the URSWHIs contribute to slightly larger mass flux compared to URSWLO
474   (Fig. 8e) during the snowband periods, likely due to slightly stronger updrafts (Table 3). For the 4
475   January case, the latter snowband accompanied less URs producing smaller bulk mass flux and
476   smaller reflectivity (Figs. 8a and 8e), likely because the URs were not clustered in space in time.
477   The upward bulk mass flux occurs within and above the moist shear instability (mRi < 0.25)
478   layers (Fig. 8d) and the layers of large vertical wind shear > 30 m s^{-1} km^{-1} (Fig. 8b, gray contour).
479   This suggests a role of shear instability for generating URs and hence upward mass transport.
480   Those were common features for the three multiband cases, (4 January first band, 16 – 17
481   December, and 1 February, shown later).
482   Figure 9a shows the vertical distributions of the URs. The total length of each bar is the
483   accumulated time with updrafts divided by the accumulated time with cloud echo as a percent at
484   each altitude bin (0.5 km). The UR accounts for more than 10% of cloud echo time at almost all
485   levels with the maximum of 31 % at 5 km altitude. The URs are classified into URSWHI and
486   URSWLO, shown by color-coded subsets along each bar. For the 4 January case, URs collocated
487   with SW > 0.4 m s^{-1} (URSWHIs) account for approximately 30% of the total number of URs above
488   the PBL height (Table 2) with the maximum at 5 km altitude. This was common for the three
489   multiband cases.
490   Figure 9b shows profiles of the occurrences (time relative to the total cloudy time) at each
491   height similar to Fig. 9a, but for wind shear > 15 m s^{-1} km^{-1} and mRi < 0.25. The midlevel UR and
492   URSWHI are well correlated with wind shear (red line, correlation of 0.76 between URSWHI and
493   wind shear). The wind shear is also correlated with the moist shear instability (mRi < 0.25,
494   correlation of 0.58). Note that the VAD-based wind data are limited to 7.8 km maximum altitude.
495   Sounding in Fig. 6c shows the shear instability (mRi < 0.25) at 8-9.5 km, consistent with local
496   peak of the UR and URSWHI occurrences.
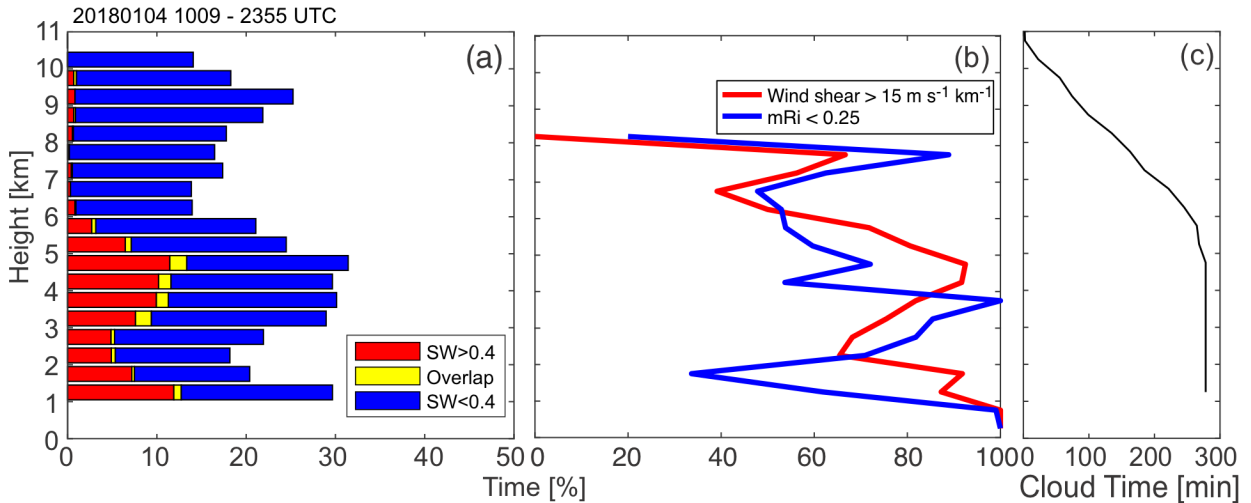
Figure 9: (a) Histograms of occurrence (time relative to the total cloudy time observed by KASPR VPT) of detected updraft regions shown as percentage of the entire cloud echo time at each altitude for the cases of 4 Jan 2018. The color bars represent different magnitudes of mean Doppler spectrum width (SW) with a SW threshold (red: SW > 0.4 m s^{-1} and blue: SW < 0.4 m s^{-1}). The SW from the KASPR VPT measurements was averaged over each updraft region. The 15-m vertical resolution data were resampled every 0.5 km height. In a resampled 0.5 km height range, some URs located in different heights can be overlapped in time. Periods where UR having SW > 0.4 m s^{-1} and UR having SW < 0.4 m s^{-1}) are overlapped in time are represented by yellow bars. (b) Occurrences of wind shear > 15 m s^{-1} km^{-1} (red), and mRi < 0.25 (blue) normalized by the entire cloud echo time at each altitude for the cases of 4 Jan 2018. (c) Profiles of the time used for the analysis at each height bin. The analysis was based on the VPT scans for 5 min duration every 15 minutes. The total analysis period is also shown in Table 1.

2). 16-17 December 2020

At 0200 UTC, surface low pressure (~1006 hPa) was along the mid-Atlantic coast and moved northward offshore during the next 24 h (orange track in Fig. 4). Similar to the 4 January case, Fig. 10 shows the horizontal distributions of the NEXRAD reflectivity at the time of snowbands, 700 hPa RAP, and the 0314 UTC on 17th sounding profile. A well-defined warm front existed to the north of the surface cyclone stretching from west to east south of Long Island, with warm advection at 700 hPa over Long Island (Fig. 10b). The WNW-ESE oriented snowbands exceeding 30 dBZ passed over SBU from south to north from 0000 to 0310 UTC 17 December (Fig. 10a). The SBU surface temperature was below freezing until 0900 UTC 17 December, while soundings at 0000, 0606, and 0715 UTC 17 December at SBU show an inversion layer and a temperature > 0°C centered around 1.5, 2.3, and 2.4 km ASL, respectively. KASPR RHI observed a melting layer after 0350 UTC 17 December at 2.5 km ASL. We focus on the period prior to the melting signature (Table 1).

524   Figure 11 shows the KASPR RHI and VPT scans near a snowband at around 01:30 UTC on
525   17th. The KASPR RHI scans (Fig. 11a-c) reveal generating cells at cloud top, with areas of
526   relatively large SW (> 0.75 m s^{-1}) from 6-7.5 km ASL, and fallstreaks extending downward to the
527   west below 6 km ASL where their directions are modified by the wind shear at around 5.4 km ASL
528   (Figs. 10c, 11b). The KASPR VPT measurements (Figs. 11d-f) also reveal updrafts with large SW
529   (> 0.4 m s^{-1}) in the generating cell layer. The cloud top generating cells are in conditionally
530   unstable layers with smaller regions of moist absolute instability layer (MAUL; Bryan and Fritsch,
531   2000) as $\partial\theta_e/\partial z < 0$ and $\partial\theta_{es}/\partial z < 0$ with $\theta_e \approx \theta_{es}$ at $6 - 6.5$ km and $6.8 - 7.0$ km ASL (Fig.
532   10c). These layers correspond to the vertical wind shear layer observed by the RHI (Fig. 11b). The
533   sounding had several layers of vertical wind shear layers (> 20 m s^{-1} km^{-1}), most of which above
534   3 km ASL were linked to shear instability (mRi < 0.25).
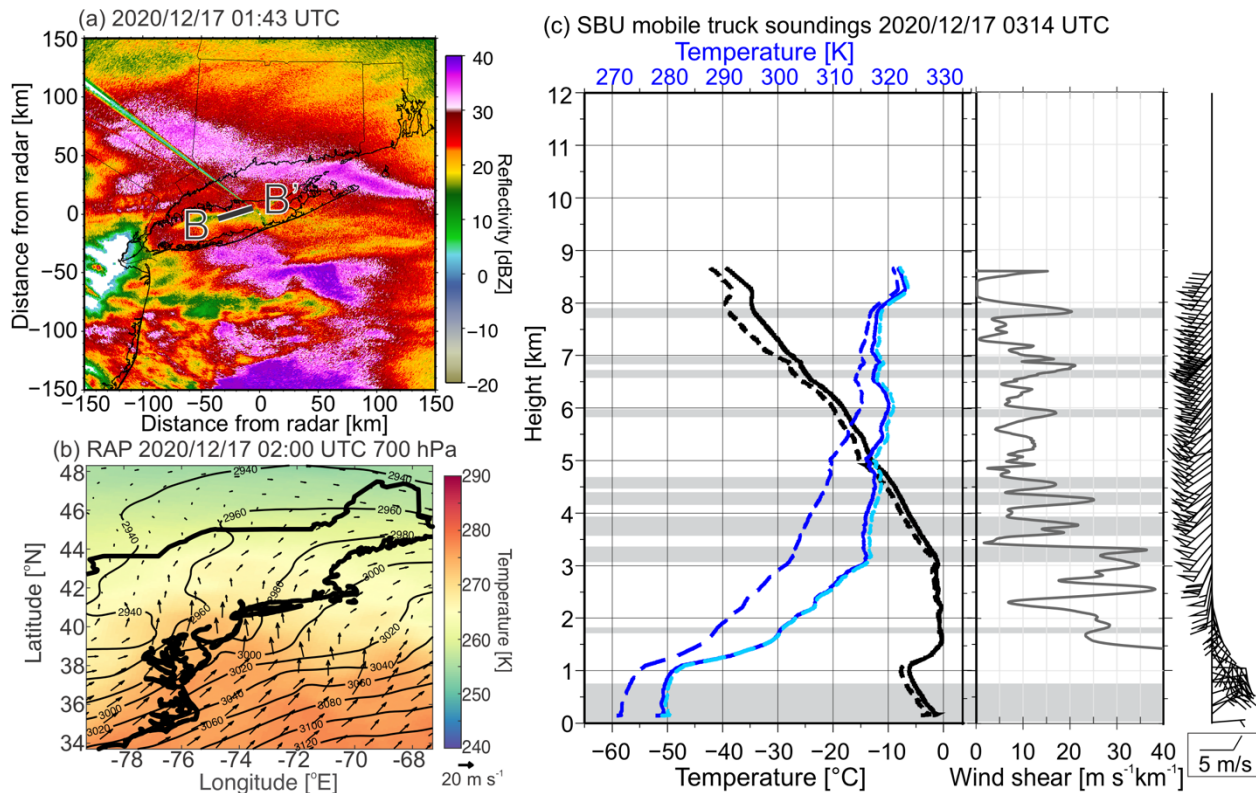
535
536   Figure 10: Same as Fig. 6 but at (a) 0143 UTC on 17 Dec 2020, (b) at 0200 UTC on 17 Dec 2020, and (c)
537   03:14 UTC on 17 Dec 2020 collected at Stony Brook (green triangle in Fig. 1). The B – B' line in (a)
538   represents the KASPR RHI direction shown in Fig. 11a-c.
539
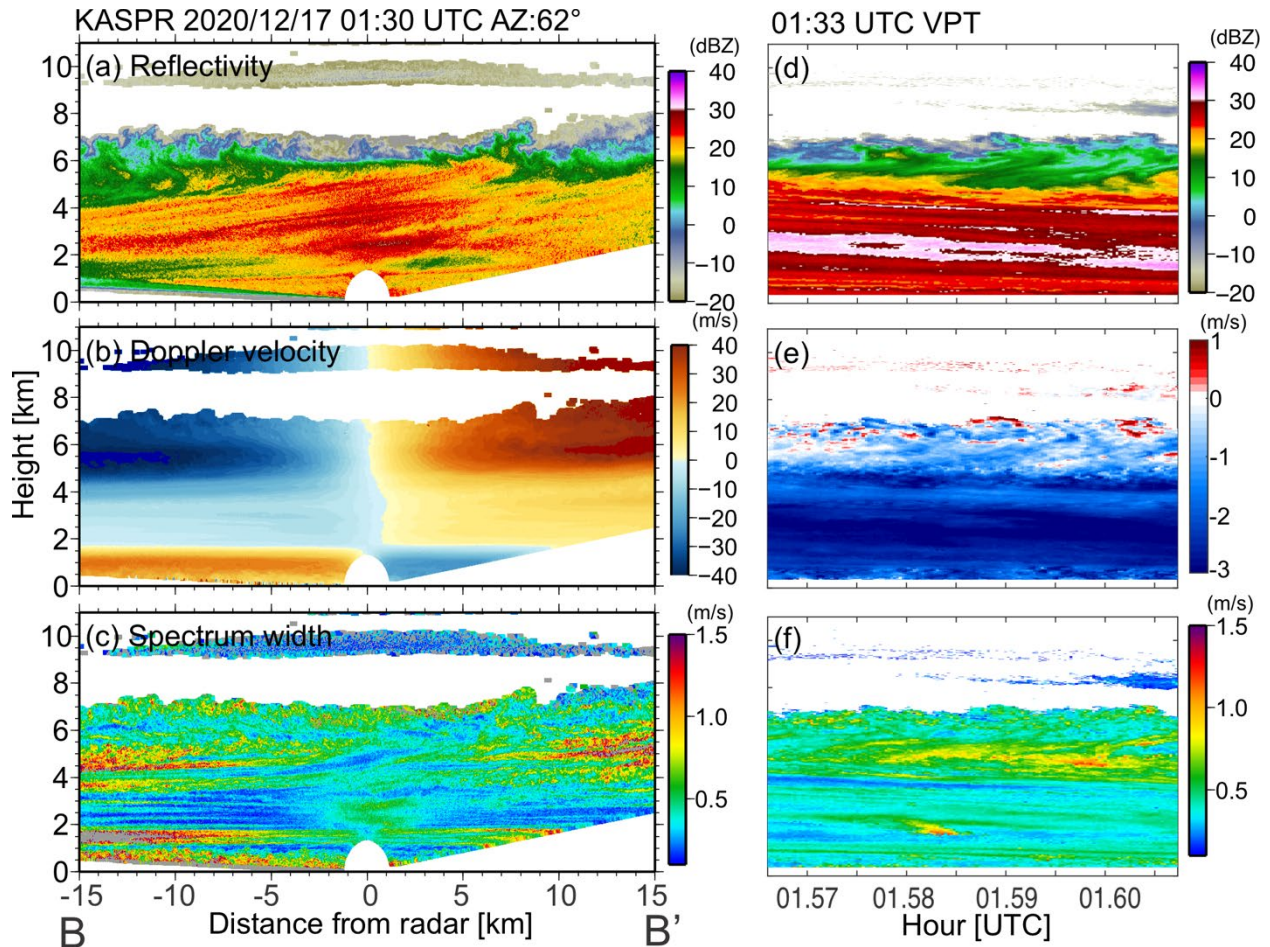
Figure 11: Same as Fig.7 but (a-c) at the 0130 UTC RHI scan along B-B' line in Fig.10a on 17 Dec 2020, and (d-f) VPT measurements on 17 Dec 2020.

Figure 12 depicts the time series of the spatial distributions of URs, horizontal wind, frontogenesis, mRi, and mass flux for the case of 16-17 December 2020, similar to Fig. 8., The snowband period is also closely associated with the 600-hPa frontogenesis, with the peak exceeding 15 K $(100 \text{ km})^{-1}$ $(3\text{hr})^{-1}$ at 0200 UTC on 17 December (Fig. 12a,c). While the URs are observed throughout the event, during the snowband period URs dominate in the cloud depth above 2 km. URSWLOs are found within 2 km from the cloud top height starting before the snowband period from 1930 UTC 16 December to 0200 UTC 17 December (Fig. 12a). URSWHIs appear from 2100 UTC 16 December just below the URSWLO layer, corresponding to the period that includes larger reflectivity >25 dBZ below 2 km (2230-0010 UTC) and below 4.5 km (0030 - 0145 UTC, snowband period). During the snowband period, URSWHIs are more prominent in a deeper layer between 4 km to the cloud top. The KASPR VAD analysis (Fig. 12b) shows that the lower boundary of the URSWHI layer well corresponds to vertical wind shear > 20 m s^{-1} km^{-1} (Fig.

556 12b) starting at 6.2 km altitude at 2100 UTC until 3-4 km at 0230 UTC and low mRi < 0.25 (Fig.

557 12d, contour).

558   In the occurrence profile in Fig. 13, similar to the 4 January case, the UR accounts for more

559 than 10% of cloud echo time at almost all levels. The maximum occurrence of URs is found at 9

560 km, but the maximum occurrence of URSWHIs is found at lower altitude around 6.5 km. The

561 occurrence profile of the wind shear in Fig. 13b is somewhat noisy, but the shear of the wind

562 direction (green line) is consistent with URSWHIs (black line, correlation of 0.33).

563   Similar to the 4 January case, the upward bulk mass flux occurs within the moist shear

564 instability (mRi < 0.25) layers (Fig. 12d). This suggests a role of shear instability for generating

565 URs and hence upward mass transport. The mass flux shows a maximum during the snowband

566 period where the URSWHIs are clustered, suggesting a contribution of URSWHIs to the upward

567 mass transport.

568
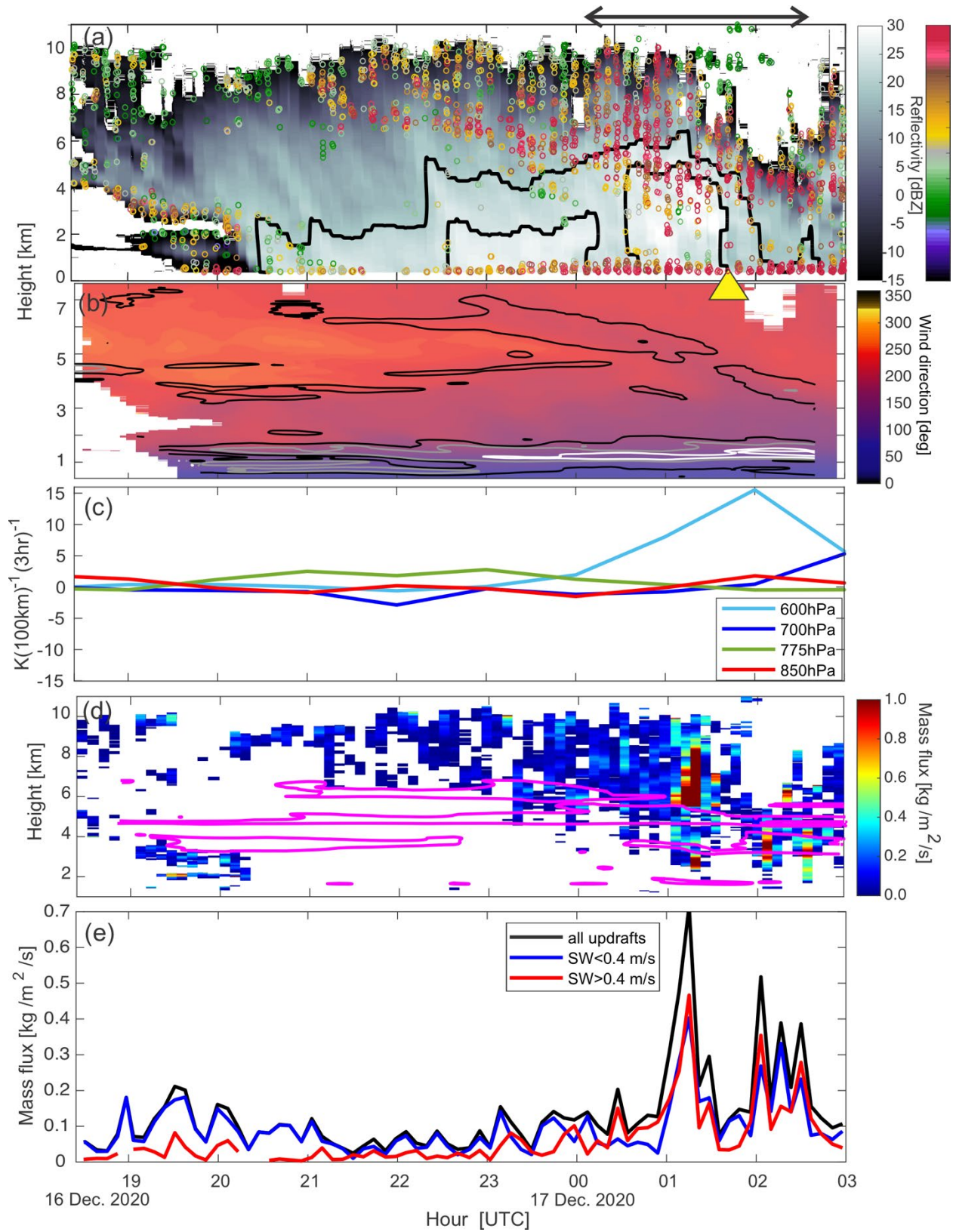
569
570   Figure 12: Same as Fig. 8, but for 16 – 17 December 2020.
571
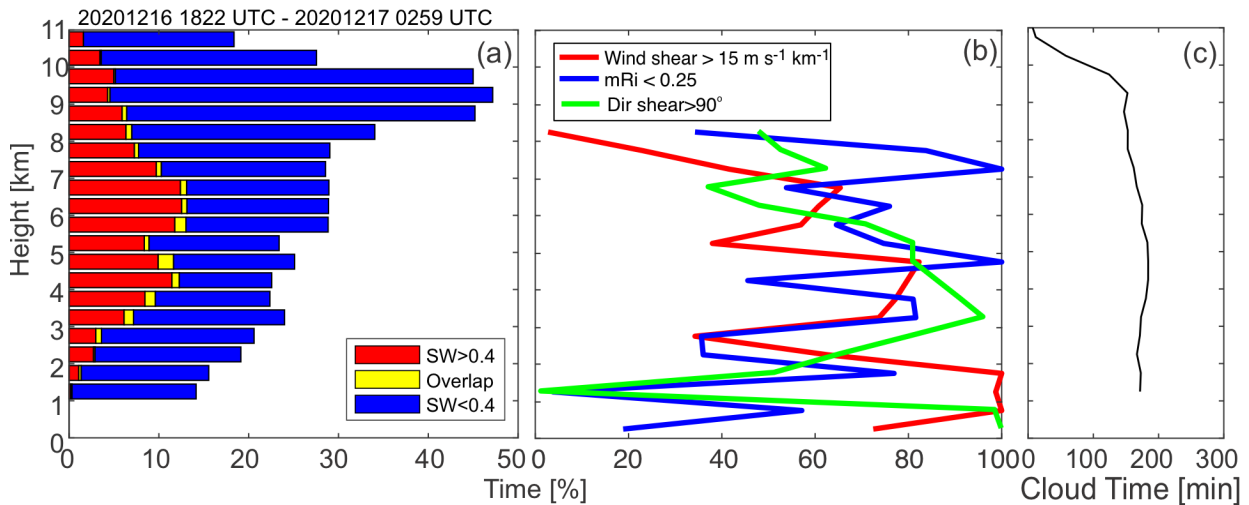
Figure 13: Same as Fig. 9, but for 16 – 17 December 2020. The occurrence of direction shear of horizontal wind > 90° km^{-1} is also shown in (b) by a green line.

3) 1 February 2021

Similar to 16-17 December, the snow event was associated with a surface cyclone moving northward to the south of Long Island (green track in Fig. 4). No snowbands were evident around Long Island before 0210 UTC 1 February. After 0210 UTC 1 February, there were precipitation areas with reflectivity > 30 dBZ around SBU, but they were not banded until 1300 UTC 1 February. From 1400 UTC to 1830 UTC 1 February, two west-east oriented snowbands (30-40 dBZ) crossed SBU moving northward (Fig. 14). As shown in Fig. 14b, there was a surface warm front just south of Long Island, with warm advection at 700 hPa over this region.

Figure 14c shows the SBU sounding at 1843 UTC 1 February near the snowband period. The sounding profile shows that a moist unstable layer exists near cloud top (4-5.2 km ASL). The KASPR RHI measurements in Fig. 15 reveal cloud-top generating cells at 5.2-7.5 km ASL near the moist unstable layer and fallstreaks to 25 dBZ underneath the generating cell layer during the snowband period (Figs. 15a,d). The Z difference between the WSR-88D and KASPR likely represents a resonance scattering effect at Ka-band owing to the presence of larger snow particles relative to the wavelength. The sounding for the generating cell layer includes moist instability, and wind shear instability (mRi < 0.25, Fig. 14c). This layer also corresponds to supersaturation with respect to ice (not shown). The VPT measurements shown in Fig. 15d-f show updrafts and large SW, indicating that the generating cells accompanied turbulence. The cloud-top generating cell layer is also well consistent with the Doppler velocity shear (Fig. 15b). Interestingly, there is

27

595 also a layer of updrafts collocated with relatively large SW (>0.4 m s⁻¹, Fig. 15e,f) at 2 km in the

596 VPT, well consistent with vertical wind shear observed by the RHI (Fig. 15b) and the sounding

597 measurements (at 2.5 km, Fig. 14c).
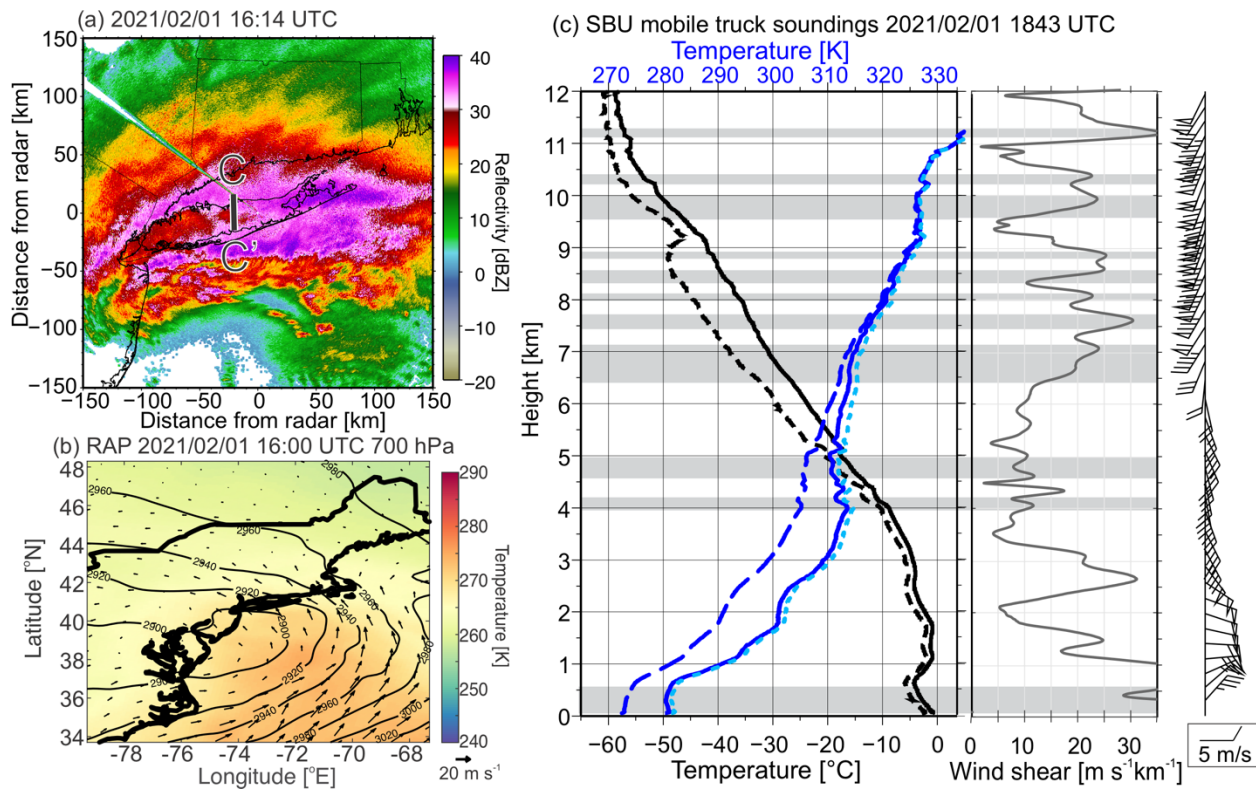
599 Figure 14: Same as Fig. 6 but at (a) 1614 UTC on 1 Feb 2021, (b) at 1600 UTC on 1 Feb 2021, and (c) 18:43
600 UTC on 1 Feb, 2021 collected at Stony Brook (green triangle in Fig. 1). The C – C' line in (a) represents the
601 KASPR RHI direction shown in Fig. 15a-c.
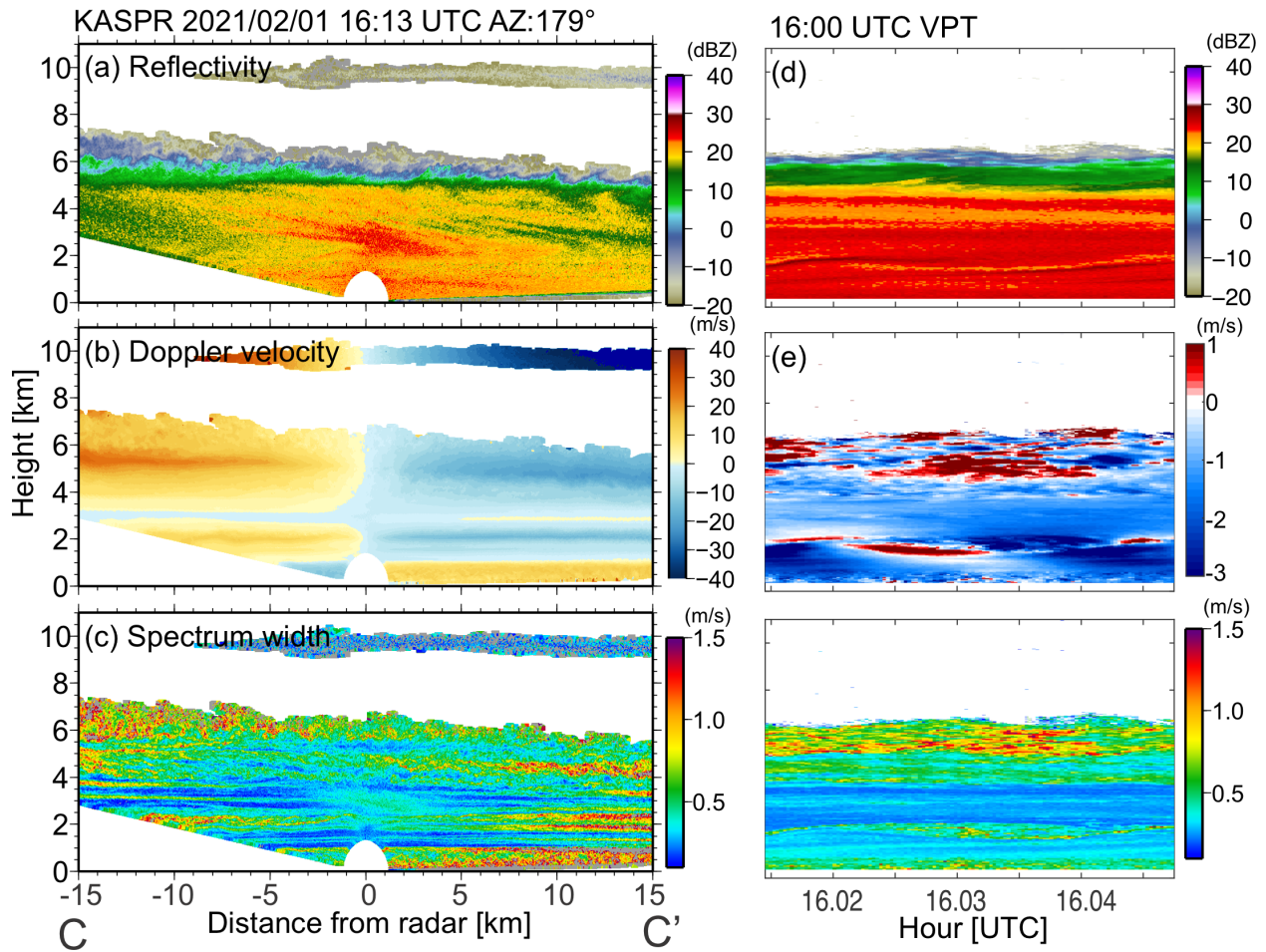
Figure 15: Same as Fig.7 but (a-c) at 1613 UTC RHIs along C-C' line in Fig.14a on 1 Feb 2021, and (d-f) VPT measurements on 1 Feb 2021.

As shown in the time series of this case shown in Fig. 16, the snowband period is associated with a 700 hPa frontogenesis of 7 K $(100 \text{ km})^{-1}$ $(3\text{hr})^{-1}$ at 1800 UTC, and the 775 hPa frontogenesis maximum of 15 K $(100 \text{ km})^{-1}$ $(3\text{hr})^{-1}$ at 2000 UTC (Fig. 16a,c). URSWLOs (represented by yellow-green dots) are observed near the cloud top with weak reflectivity ($<\sim0$ dBZ) from the beginning of the observation on 31 January (1800 UTC) until 1300 UTC on 1 February. URSWHIs occur from 1200 UTC 1 February to the end of the analysis period (0000 UTC 2 February), which is consistent with the snowband period. The KASPR VAD analysis (Fig. 16b) shows the vertical wind shear produced by south-southeasterly wind in the low altitudes and southwesterly wind in the upper altitudes. The shear line is found between 2 and 3 km altitudes until 1210 UTC on 1 February and then ascends to 6 km altitude by 1400 UTC. The low-level south-southeasterly wind corresponds to the 700 hPa warm advection presented in the RAP data at 1400 UTC (Fig. 14b).

29

618   In the occurrence profile in Fig. 17, similar to the other multiband cases, the UR accounts for

619   more than 10% of cloud echo time at almost all levels with the maximum of UR (and URSWLO)

620   occurrence is found near the cloud top. The maximum occurrence of URSWHIs is found at lower

621   altitude around 7 km, and the second peak is found at around 3 km. These peaks in the URSWHI

622   occurrence are well consistent with the peaks of the occurrence of large wind shear (red line,

623   correlation of 0.24 with URSWHI). The URSWHI occurrence is also well correlated with low mRi
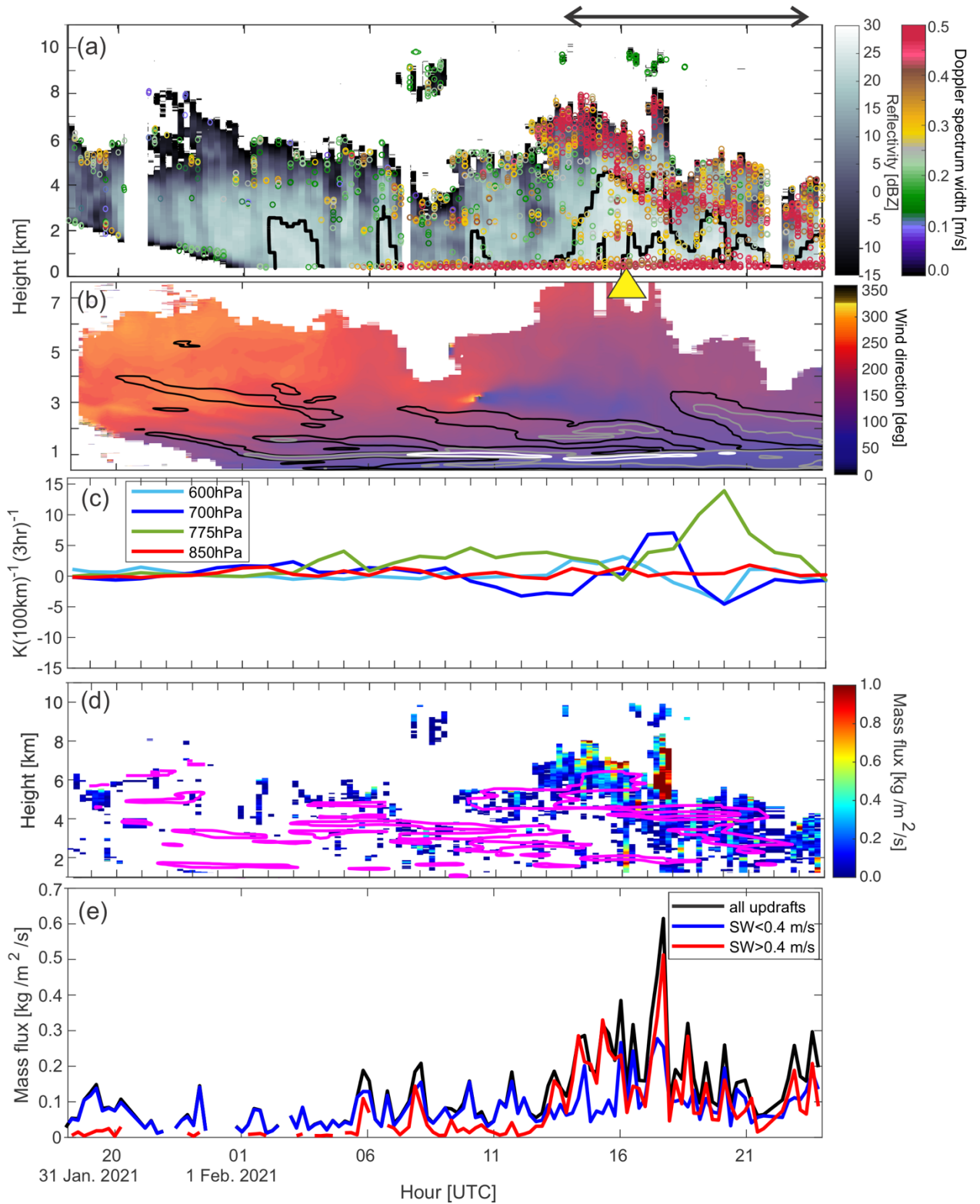
624   (correlation of 0.63).

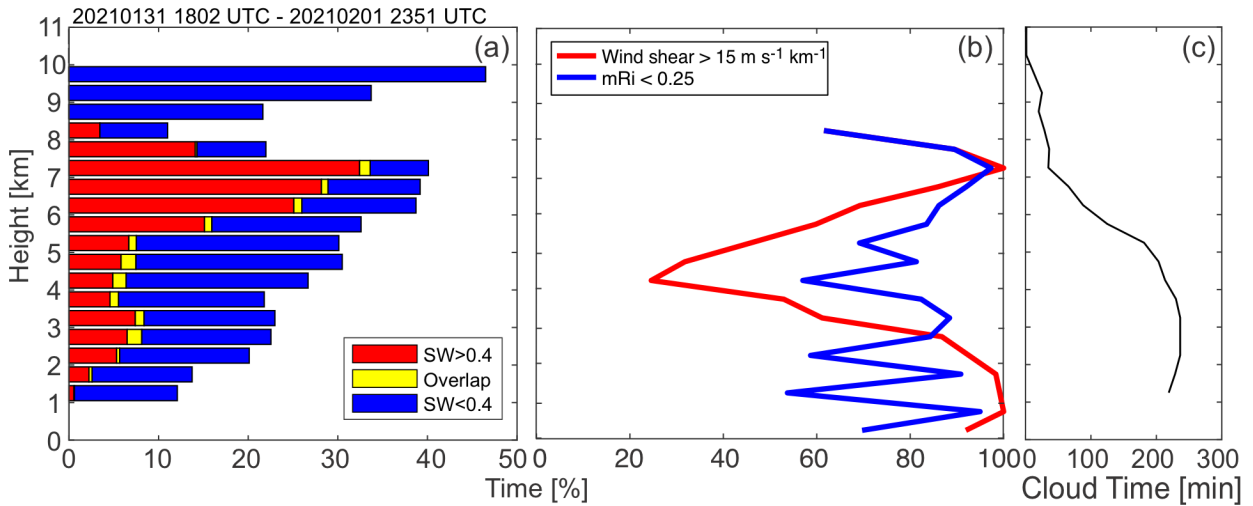Figure 16: Same as Fig. 8, but for 31 January – 1 February 2020.

Figure 17: Same as Fig. 9, but for the case of 1 Feb 2021.

4) 18 January 2020

For the 18 January case, which accompanied a single snowband, by 0300 UTC 19 January, the surface warm front associated with a surface cyclone (~1003 hPa) centered over northern Michigan was southwest of Long Island along the mid-Atlantic coast as the storm center moved eastward (magenta track in Fig. 4). The vertical wind shear seemed similar to the multiband cases, but the spatial distributions of UR and the radar reflectivity showed some differences. Figure 18 shows the horizontal distributions of the NEXRAD reflectivity at the time of snowbands, 700 hPa RAP, and the 1813 UTC sounding profile. The warm-frontal snowband (> 20 dBZ) orientated from northwest to southeast crossed SBU between 1830-2015 UTC 18 January (Fig. 18a) accompanying a 700-hPa warm advection (Fig. 18b). The maximum WSR-88D reflectivity for this snowband (~30 dBZ) was 5-10 dB weaker than the other cases. The surface precipitation transitioned to rain after the warm frontal snowband passage. This study focuses on the warm frontal snowband to avoid uncertain errors associated with hydrometeor attenuation in the rain layer.

The sounding from the SBU mobile truck deployed at Cedar Beach (blue triangle of Fig.1) at 1813 UTC 18 January, which was closest to the snowband passage, shows a warm-frontal stable layer with veering winds from 1-2 km ASL and a near moist neutral layer from 2-3 km ASL (Fig. 18c). The sounding in Fig. 18c and KASPR measurements in Fig. 19 suggest that the cloud top height reach 10 km ASL, where the vertical profile is less stable and near moist neutral (7-10 km ASL). KASPR RHI scans oriented NE-SW (B-B' in Fig. 18a) and crossing the snowband (Figs. 19a-c) reveal a gradual increase of reflectivity toward the surface above ~3 km ASL and relatively

651 uniform reflectivity at a given altitude when the snowband passed. The VPT measurements (Figs.

652 19d-f) do not show significant convection above 4 km, where the RHI Doppler velocity shows less

653 vertical wind shear. There is a wave-like feature at the radar echo top (at ~10 km, Figs. 19a,b,c,e)

654 with weak reflectivity, which could be a source of precipitation. The VPT measurements show

655 layers of relatively large SW at 2 and 4 km. These layers also correspond to the vertical wind shear

656 observed by the RHI and shear unstable layers observed by the sounding (mRi < 0.25, gray shades).

657 The lower layer (2 km ASL) corresponds to a local intensification of reflectivity (~25 dB). These

658 SW values, however, weaker (generally < 0.4 m s^{-1}) than the other cases (Fig. 19f).
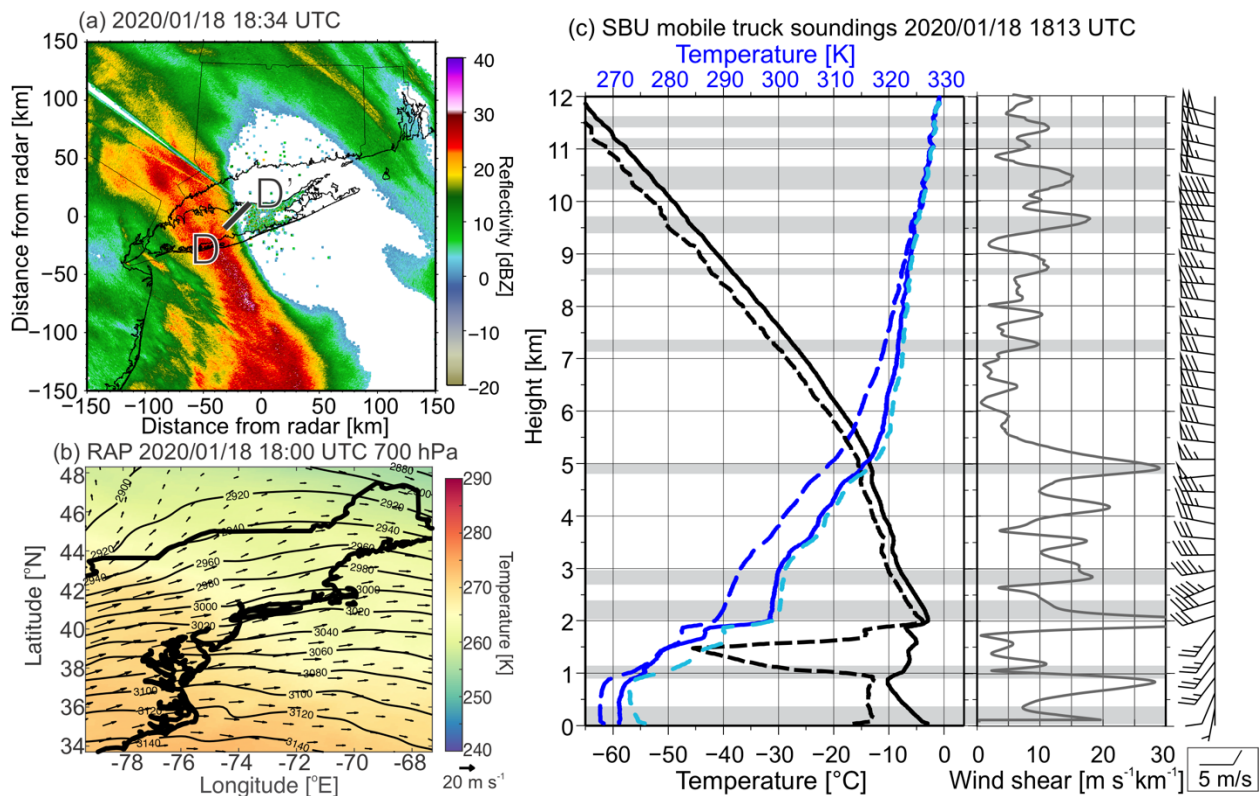
659
660 Figure 18: Same as Fig. 6 but at (a) 1834 UTC on 18 Jan 2020, (b) at 1800 UTC on 18 Jan 2020, and (c) 18:13
661 UTC 18 Jan 2020 collected at Cedar Beach (blue triangle in Fig. 1). The D – D' line in (a) represents the
662 KASPR RHI direction shown in Fig. 19a-c.
663
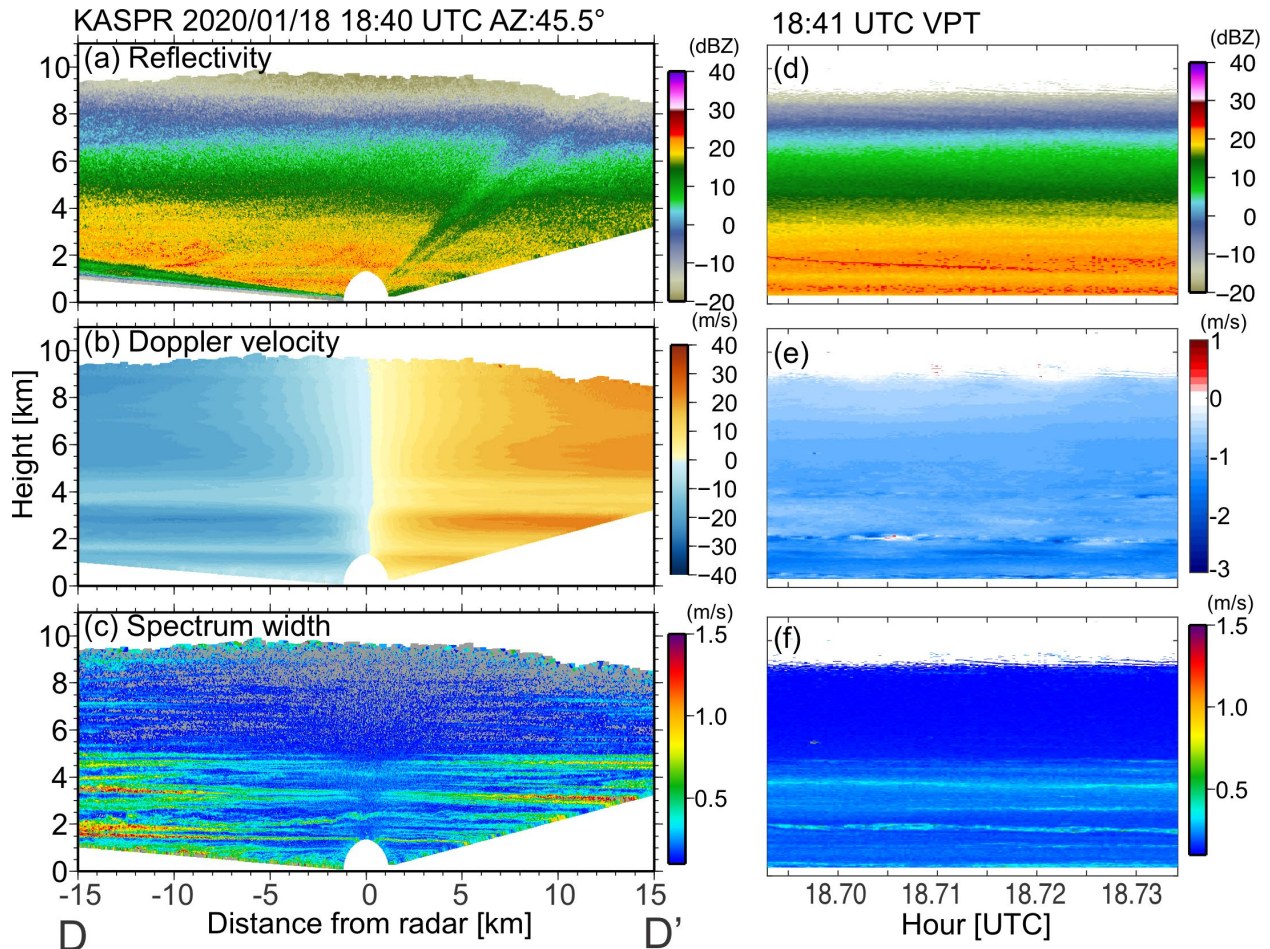
664
665 Figure 19: Same as Fig.9 but (a-c) at the 1840 UTC RHI scan along D-D' line in Fig. 18a on 18 Jan 2020 and
666 (d-f) VPT measurements on 18 Jan 2020.
667

668   Figure 20 shows the set of time series for the 18 January case. Similar to the other three cases,

669 URSWLOs (represented by yellow-green-blue dots) are observed near the cloud top with weak

670 reflectivity (< 0 dBZ), but the frontogenesis was very weak at all levels (< 2 K (100 km)$^{-1}$ (3hr)$^{-1}$

671 at 700, 775, and 800 hPa, Fig. 20c). Multiple layers of vertical wind shear > 30 m s^{-1} km^{-1} (Fig.

672 20b) are observed within the cloud, similar to the other three cases. In contrast to the three

673 multiband cases, for the 18 January case, no significant increase in the mass flux is found (Fig.

674 20d,e). Near the cloud top, where URSWLOs dominate, the mass flux varies in magnitude and is

675 discontinuous in time.

676   Figure 21 shows the occurrence profiles. The UR accounts for less than or equal to 10% of

677 cloud echo time 2.5 km, and URSWHI accounts for only 3% at all levels (Fig. 21a). Although the

678 number of URSWHIs is small, the occurrences of UR and URSWHI are correlated with the large

679 wind shear (red line, correlation of 0.48 with URSWHI, Fig. 20b). They are also weakly correlated

34

680   with shear instability; the correlation between UR (gray line) and low mRi (blue line) is 0.30, and

681   that between large wind shear (red line) and low mRi (blue line) is 0.57. While the layers of updraft

682   regions and wind shear were correlated, the strength of wind shear or shear instability might not

683   be a factor of the strength and frequency of the updrafts. Further analysis is needed to evaluate this

684   using high resolution model simulations.
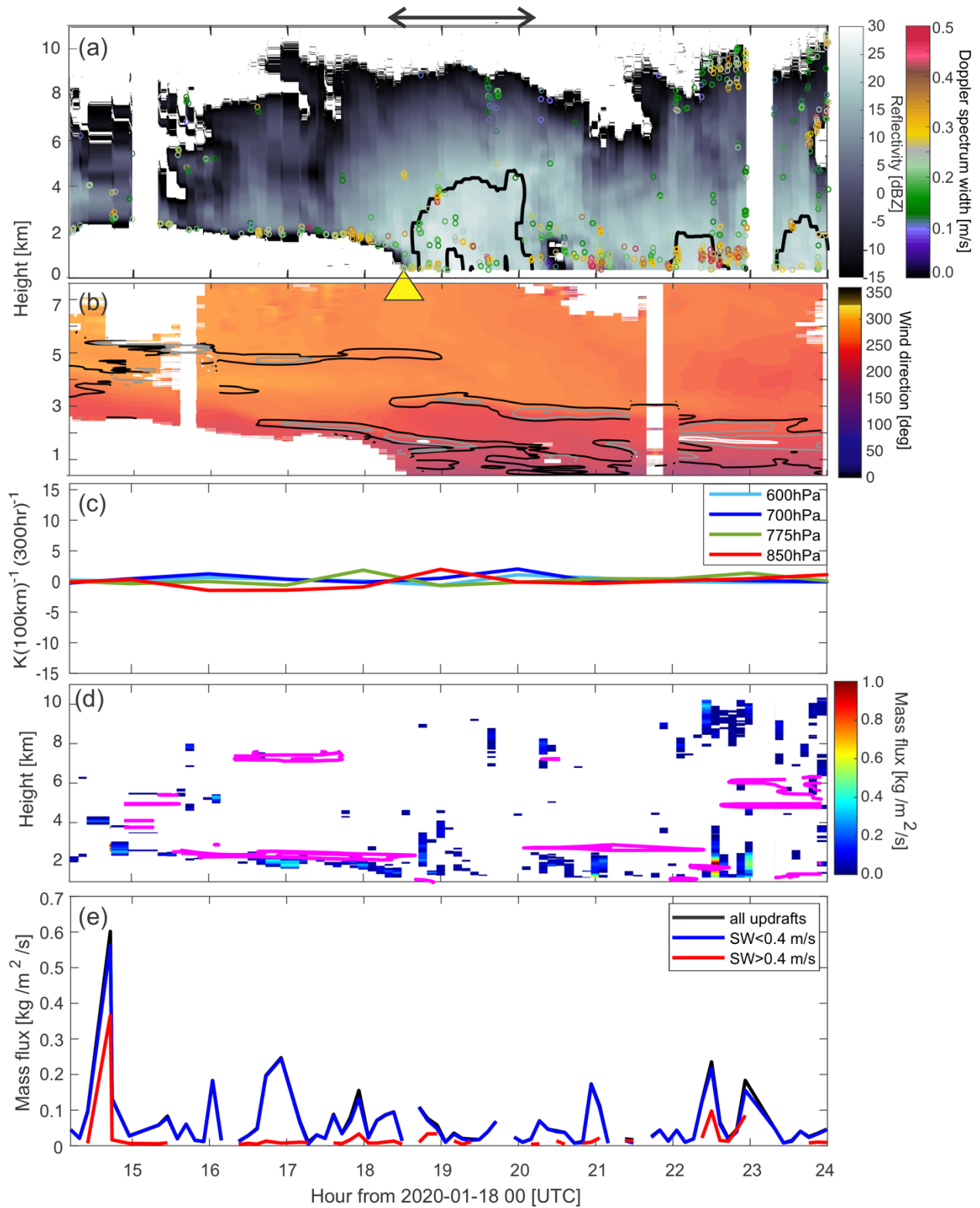
Figure 20: Same as Fig. 8, but for 18 January 2020.
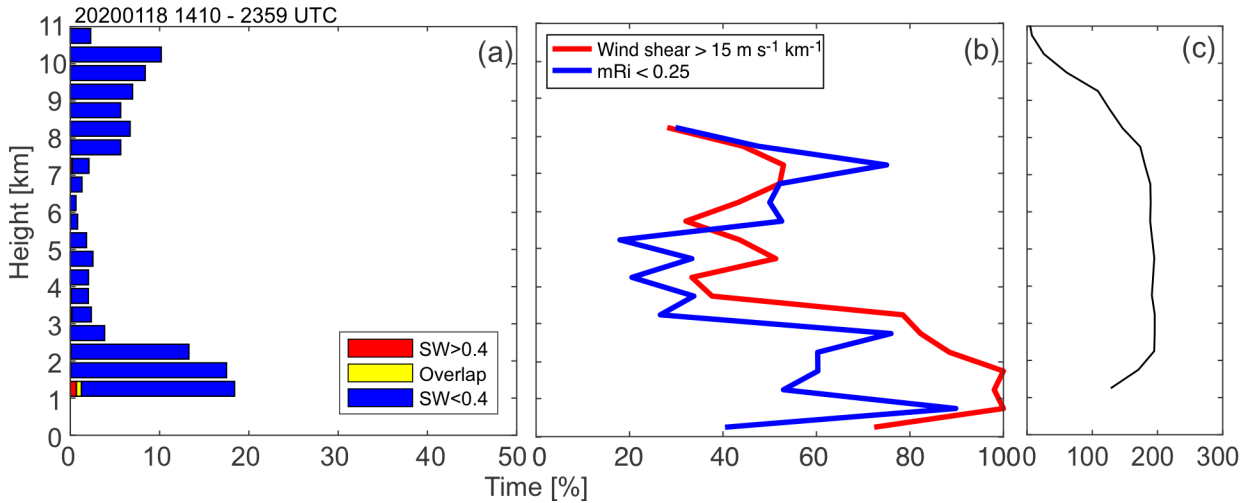
Figure 21: Same as Fig. 9, but for the case of 18 January 2020.

c. Summary

The snowbands accompanied convective cells near cloud top and fallstreaks underneath, as observed by the previous studies. The convective cells were well collocated with layers of updrafts and large SW associated with vertical wind shear. They suggest that the near cloud top convective cells (i.e., generating cells) contributed to the precipitation within the snowbands. The weak snowband case (18 January) did not show significant updrafts and turbulence (large SW) near the cloud top even within the cloud layer. The URs associated with wind shear was often multi-layered in the precipitating clouds, as it was observed not only near the cloud top but also the middle of the precipitating clouds. They were collocated with intensification of the precipitation underneath as measured by reflectivity.

Although there is a case-to-case variability in the heights, the URs collocated with SW>0.4 m s^{-1} (URSWHIs) occur in more interior clouds of the multiband cases. URSWHIs tend to be shorter lived compared to the URSWLOs for all cases (approximately 1 – 2 sec shorter, Table 3). URSWHIs have slightly (0.20 – 0.52 m s^{-1}) stronger median upward motion and 3.5 – 16.4 dB larger median reflectivity (Table 3). In contrast, URs collocated with SW<0.4 m s^{-1} (URSWLOs) show higher frequencies at higher altitudes. They are found above 8 km altitude; some of them are found very close to the echo tops, and most of them are found within 1-2 km distance from the echo tops. The lower SW is likely due to a combination of less turbulence and a narrower particle size distribution owing to weaker reflectivity. The peak of the URSWHI occurrence is found at a lower altitude than that of the URSWLOs.

710   Overall, URs are found throughout the snowstorms regardless of the snowband periods or
711   frontogenesis for the four cases. The occurrences of URs and URSWHIs are well correlated with
712   large wind shear and shear instability (Figs. 9, 13, 17, and 21). The URSWHIs are frequently found
713   during the snowband periods for three of the cases.

714
715
716
717
718   4. **Discussion**

719   Novel high-vertical resolution, high-sensitivity vertically-pointing radar measurements in four
720   winter storms along the US northeast coast showed that URs are ubiquitous features in the winter
721   storms. They are correlated with layers of enhanced wind shear and are found frequently in the
722   presence of snowbands, which suggests that URs could promote precipitating particle growth.
723   They accompanied the snowbands, but they also occurred outside the snowbands. This suggests
724   that the URs could promote precipitating particle growth. In particular, high-reflectivity bands
725   from 4 January, 16-17 December, and 1 February accompanied URSWHIs. They suggest that URs
726   associated with the wind shear contributed to the formation and /or intensification of snowbands.
727   This is consistent with the previous studies (e.g., Plummer et al. 2014; Rauber et al. 2014). The
728   present study revealed that the URs contributed to particularly significant upward mass flux when
729   they were clustered in space and time especially during the snowband periods. RAP 700 hPa
730   specific humidity > 5 g kg^{-1} (not shown) was associated with periods with the larger mass flux in
731   all four cases. It is suggested that the URs could play a role as a driver for supplying water vapor
732   that could produce saturation with respect to liquid water and thus potentially the formation of
733   supercooled liquid droplets. They could then contribute to forming/growing precipitation particles,
734   as pointed out by Plummer et al. (2014). The URs were observed not only in the snowbands, but
735   also outside the snowbands, although they were distributed sparsely compared to within the
736   snowbands. This suggests a role of the URs on snow particle formation and/or intensification of
737   snowfall outside the snowbands.
738   The URs, especially URSWHIs were well correlated with vertical wind shear and shear
739   instability (mRi<0.25, Figs. 8, 9, 12, 13, 16, 17, 20, and 21), suggesting that vertical wind shear
740   caused turbulence, which included upward vertical velocity perturbations identified here as URs.
741   The large mass flux is particularly associated with the moist shear instability, suggesting a role of

the turbulence induced URs on the vertical mass transport. The wind shears were multi-layered in the cloud systems. This is consistent with the former studies such as Boucher et al. (1965), Wexler et al. (1967), Sylett et al. (1995), and Rauber et al. (2014) that observed wind shears associated with frontal zones in winter storms using Doppler radar measurements. This suggests that the snowstorm systems in the present study were composed of several air masses originating from different sources producing frontal zones, as commonly observed by previous studies (e.g. Boucher et al. 1965; Rauber et al. 2014). The KASPR measurements presented in this study also showed wind shear layers with low mRi outside the frontal zones. The multi-layers of turbulence and updrafts associated with wind shear observed by the RHIs and soundings in this study suggest the presence of smaller scale air masses rather than synoptic scale air masses as presented in Rauber et al. (2014).

It is hard to determine the role of frontogenesis in the UR formation, because frontogenesis, larger (synoptic) scale forcing, associates larger scale ascending that generally has smaller (cm s^{-1} scale) vertical air motion. The URs and updrafts observed by the vertically-pointing radar measurements in this study are finer scales having ~10 s duration and > 1 m s^{-1} upward velocity than those associated with frontogenesis.

It is possible that the updrafts at the cloud tops could be produced in part by instabilities caused by cloud-top radiative cooling. The cloud-top cooling could produce cloud-top destabilization leading to development of generating cells (e.g., Sylett et al. 1995; Keeler et al. 2016). That cooling might pair with heating associated with snow particle growth (depositional and riming growth) within the cloud, resulting in lapse rate maintaining convection (Kumjian et al. 2014). Alternatively, if there was advection of drier and/or cooler (i.e., lower θ_e) air aloft, it could play a role in producing the potential instability, as shown in the soundings from the 16-17 December and 1 February cases. Future studies should examine the relative roles of microscale updrafts as compared to mesoscale and synoptic scale updrafts.

The wind-shear instability (i.e. Kelvin–Helmholtz instability) can also produce downdrafts, which are not focused on in this study. The updrafts can contribute to supplying water vapor producing water saturation and supercooled water in the cells and hence enhancement of particle growth and snow intensification (Plummer et al. 2014; Kumjian et al. 2014), while the downdrafts can play a role in entrainment and sublimation (Rauber et al. 2014). The downdraft regions in this study were found between URs at midlevels and near the cloud tops (e.g., Figs. 11, 15). The spatial

773 distribution of the downdraft regions was very similar to that of URs, except near the cloud tops.
774 This suggests that URs existed as a UR and downdraft region in the midlevels of the storms. The
775 midlevels of the storms could be supersaturated, then precipitation particles did not have a chance
776 of much sublimation within the downdraft regions. Near the cloud tops, detecting downdraft
777 regions by the radar measurements might be difficult because hydrometeor particles could be
778 sublimated. Considering the microphysics within the updraft/downdraft regions near the cloud tops
779 and at midlevels should be important to analyze mass/water budgets and entrainment and
780 understand the water cycle within the cloud systems. We will need lidar measurements to observe
781 the clear-air updrafts and downdrafts and high-resolution simulations that resolve the microscale
782 updrafts and downdrafts.

783　　Limited cases in this study (four cases) result in some uncertainty in the relationships between
784 URs and wind shear. Analysis including more cases using the high-resolution radar observations
785 can help to better understand the formation mechanisms of URs and the roles of URs in
786 microphysical processes in winter storms. Model simulations will help to further understand the
787 mechanisms of UR generations and the microphysical impacts including the sources of multi layers
788 that generate turbulence and ice particle formation, if the models can resolve the wind shear layers
789 and use optimal turbulence kinematic energy parameterization. The model simulations are beyond
790 the scope of this observational study.

791　　The methodology to identify microscale updrafts described in this paper can be applied to other
792 vertically-pointing Doppler radar datasets to examine the small scale velocity structures that are
793 too fine scale to be resolved by other sensors such as the US National Weather Service PPI
794 scanning radars. Further analysis of microscale updrafts and downdrafts can also shed light on the
795 degree to which ice precipitation mass changes in a more episodic mode (smaller time and space
796 scales) versus a more continuous mode (longer time and scale scales) in winter storms and in
797 stratiform regions. The spatial/time scales of the updrafts in this study are larger than the radar
798 sampling volume (~15 m in height and ~1 s in time). There can be smaller scale turbulence (i.e.
799 eddies) within the sampling volume, which can be observed by higher resolution radars/lidars
800 (having a few cm scale resolution, Schmidt et al. 2012; Cooper and Chattopadhyay 2014).

801

802　　5. **Summary**

803   Although microscale upward motions in the snowstorms could play an important role in snow
804   precipitation, their characteristics relative to the snowbands and relationship with vertical wind
805   shear instability from Kelvin–Helmholtz instability has not been shown yet. We investigated the
806   relations among microscale updraft regions (URs) and snowbands, vertical wind shear, shear
807   instability, and frontogenesis, and roles on vertical mass transport for four winter snowstorm cases
808   (4 January 2018; 18 January 2020; 16-17 December 2020; 1 February 2021). Measurements were
809   made as each storm passed over the Stony Brook and Brookhaven National Laboratory Radar
810   Observatory (SBRO) in Stony Brook, NY and included periods with and without snowbands and
811   in the northwest and northeast quadrants of the three storms (4 January, 16 – 17 December, and 1
812   February) and the southwest quadrant of the 18 January storm. Three of the cases (4 January, 16 –
813   17 December, and 1 February) included more than one snowband.

814   The mean Doppler velocity from the vertically-pointing Ka-band polarimetric radar
815   measurements was used to identify updraft regions in this study. After the removal of hydrometeor
816   sedimentation from the VPT measured mean Doppler velocity, the updraft region was simply
817   defined as a region with the estimated vertical air motion (VPT measured mean Doppler velocity
818   minus estimated particle fall speed) greater than or equal to 0.4 m s^{-1} (negative sign of Doppler
819   velocity indicates a downward motion). Using vertically-pointing radar data does not provide
820   information on the lifecycle of the updrafts, but the duration of the updraft overhead can be
821   converted to an estimated spatial scale using horizontal wind estimated from a KASPR PPI VAD
822   technique. We estimated mass flux based on the detected updraft regions and sounding data and
823   investigated relationships among updraft regions, mass flux, and frontogenesis, and shear
824   instability to discuss roles of mesoscale instability on generating the updrafts and vertical mass
825   transport. We summarize the characteristics of the updraft regions and their associations with
826   spectral width, wind shear and frontogenesis:

827   ● In the vertical pointing radar data, the distribution of updraft durations is approximately
828   logarithmic with most individual updrafts passing overhead in only a few seconds (<20
829   sec) (Fig. 5a). They are roughly equivalent to spatial scales < 500 m. The aspect ratio
830   of the updraft regions estimated from the duration and horizontal scale has a lognormal
831   frequency distribution with a modal value near 1 (equivalent to circular, Fig. 5b).

832   ● Overall, the snowbands occur in a region of low to mid-level frontogenesis, but the
833   microscale updraft regions are found at all altitudes, occur both in regions with and

834   without snowbands. (Figs. 8a, 12a, 16a, and 20a). They suggest a role of the microscale

835   updraft regions on snow particle formation /or intensification of snowfall not only in

836   the snowbands but also outside the snowbands.

837   ●   The subset of updraft regions with larger VPT Doppler spectrum width (SW > 0.4 m s[-]

838   [1]), which imply more turbulent updrafts, frequently occur within mid-levels of the

839   storms (several km below cloud echo top). They are associated with vertical wind shear

840   and moist shear instability that are sometimes multi-layered in the precipitating clouds.

841   They suggest that the updraft regions can be triggered in the shear unstable layers (Figs.

842   9, 13, 17, and 21).

843   ●   Updraft regions that tend to be closer together in space and time yield more bulk mass

844   flux. The duration of individual updraft regions is not the primary factor of the mass

845   flux (Figs. 8e, 12e, 16e, and 20e).

846   ●   The calculated upward bulk mass flux occurs within and above the moist shear

847   insurability layers. The highest mean mass flux is produced during snowband periods

848   (Figs. 8d, 12d, 16d, and 20d).

849   The analysis implies that the dominant forcing of the microscale updrafts appears to be

850 associated with the vertical shear instability. The updrafts are responsible for upward mass flux

851 and then contribute to the precipitation mass growth regardless of whether snowbands are present

852 or not. We also detected many microscale updrafts in the boundary layer during portions of each

853 of the four storms but did not focus on them in this study. These low-level updrafts may further

854 modify the microphysics and would be an interesting topic for future studies. Future studies with

855 increasing cases should examine the relative roles of microscale updrafts, downdrafts, and

856 turbulence as compared to mesoscale and synoptic scale updrafts and quantitatively estimate the

857 contributions to the mass growth to better understand the precipitation production in winter storms,

858 which in turn may aid in reducing uncertainties in snowfall accumulation forecasts.

859

860

861 **Appendix A**

862   There are six major Doppler spectral broadening mechanisms that contribute to the measured

863 spectrum width σ_{tot} (Doviak and Zrnić, 2006): dispersion of hydrometeor fall speed σ_{psd},

864 turbulence σ_{tur}, mean horizontal wind shear σ_{shr}, cross wind σ_{crs}, antenna motion σ_{ant}, and

865   parameters related to the particle orientation (including canting, horizontal orientation, wobbling,

866   and oscillation of shape, Dunnavan, 2021) σ_{ori}. Those contributions can be written as:

867
$$\sigma_{tot} = \sqrt{\sigma_{psd}^2 + \sigma_{tur}^2 + \sigma_{shr}^2 + \sigma_{crs}^2 + \sigma_{ant}^2 + \sigma_{ori}^2} \qquad (A1)$$

868   To simplify, the contributions of σ_{ant} and σ_{ori} are ignored, assuming that they are negligible

869   compared to the other terms. Moreover, for the VPT measurements, σ_{shr} and σ_{crs} can also be

870   negligible compared to σ_{psd} and σ_{tur}. The value of σ_{shr} in Eq. A1 differs from the original

871   surveillance-scan form proposed by Doviak and Zrnić (2006) because we neglect possible

872   contributions from vertical wind shear across the sampling volume; only the horizontal wind shear

873   component is considered here. For the VPT measurements in this study, we consider the σ_{psd} and

874 σ_{tur} to evaluate the contributions to σ_{tot} as:

875
$$\sigma_{tot} = \sqrt{\sigma_{psd}^2 + \sigma_{tur}^2} \qquad (A2)$$

876   In the case of VPT measurements, σ_{tur} in Eq. (A2) can represent the dispersion of radial velocities

877   within the sampling volume owing to turbulent structures and/or horizontal gradients in coherent

878   vertical structures. To estimate general σ_{psd} for the present cases, Fig. A1a shows a frequency

879   distribution of SW versus reflectivity from the KASPR VPT measurements collected during the

880   selected four events in this study. In this figure, we assume that σ_{psd} can be correlated with

881   reflectivity statistically. The SW with the maximum frequency at each reflectivity bin increased

882   with reflectivity. This can represent statistical σ_{psd} associated with reflectivity. For the four cases,

883   which are stratiform snow events, radar reflectivity generally increases with decreasing height,

884   suggesting that hydrometeor particles generally grow downward. As the particle size distribution

885   broadens with increasing reflectivity, σ_{psd}, which is attributed to the spread of particle fall speeds

886   in the radar resolution volume can also increase. The SW with maximum frequency is generally

887   less than 0.2 m s^{-1}. Figure A1b shows vertical frequency distribution of the SW. The SW with

888   maximum frequency increases downward and is generally less than 0.2 m s^{-1}.

889   Figure A2 shows the relationship of Eq. A2 to represent the contributions of σ_{psd} and σ_{tur} to

890   σ_{tot}. At σ_{tot} (observed SW) = 0.3 m s^{-1} with σ_{psd}= 0.2 m s^{-1}, σ_{tur} is approximately 0.2 m s^{-1},

891   comparable with σ_{psd}. For σ_{tot} > 0.35 m s^{-1} with σ_{psd}= 0.2 m s^{-1}, σ_{tur} > σ_{psd}, indicating that σ_{tur}

892   can be a primary contribution to the observed SW. We use σ_{tot} = 0.4 m s^{-1} for the threshold of

893   observed SW to classify detected updraft regions related to turbulence. When we compared

894   statistics using a threshold of σ_{tot} = 0.4 m s^{-1} and a threshold of 0.5 m s^{-1}, the medians of duration
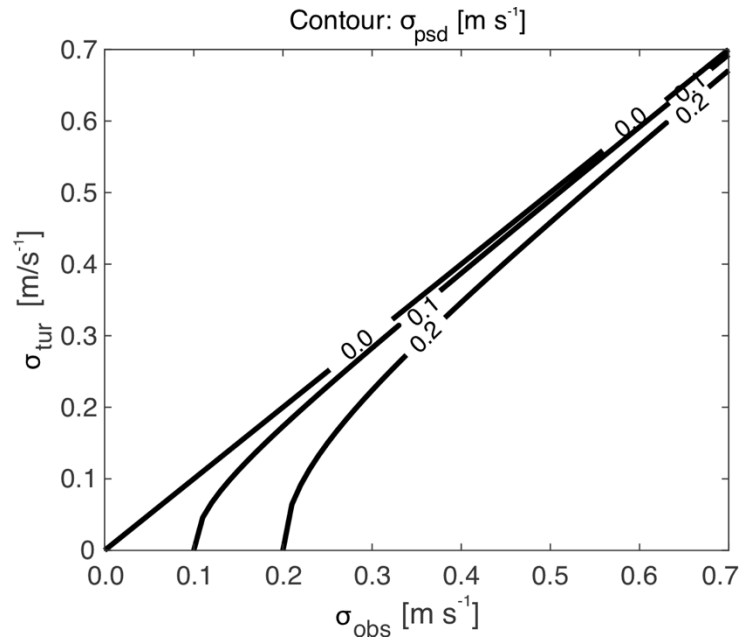
895   and vertical extent for URSWHI and URSWLO did not change much (less than 1 sec and less than
896   15 m, respectively). The medians of reflectivity and upward motion slightly increased as we
897   expected; median reflectivity for URSWHI increased by ~0.5 dB and that for URSWLO increased
898   by ~2 dB, and median upward motions for both URSWHI and URSWLO increased by less than
899   0.05 m s^{-1}.

900

901

902
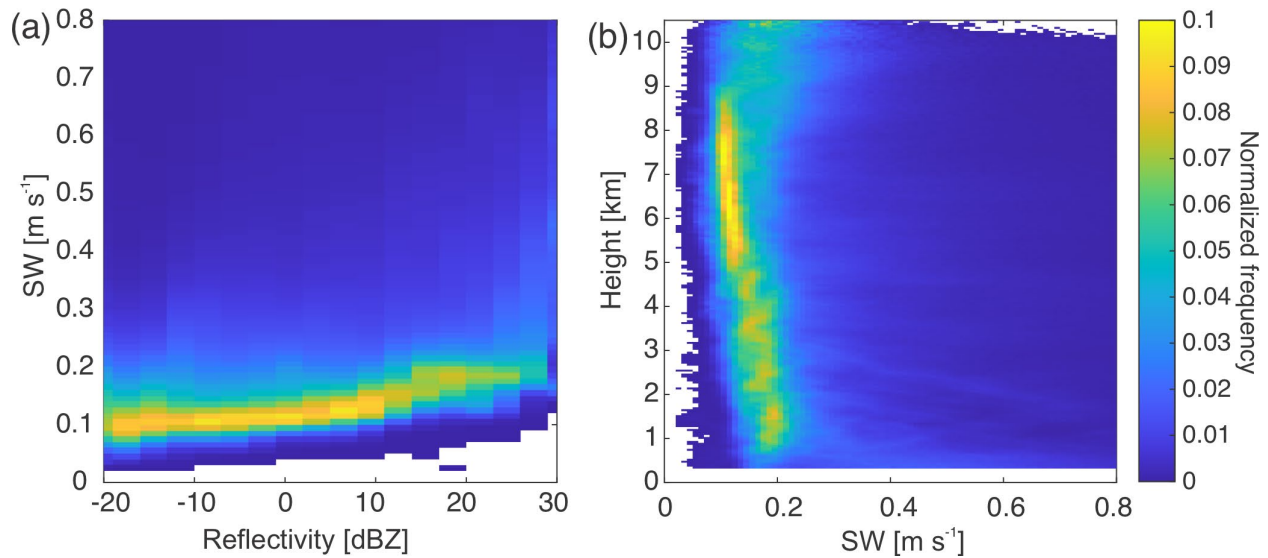
903   Figure A1: (a) Frequency distribution of SW versus reflectivity from the KASPR VPT
904   measurements collected during the four events. Color shade represents the frequency normalized
905   every 2 dBZ from -20 dBZ. (a) Frequency by altitude distribution of SW. Color shade represents
906   the frequency normalized at each radar range-gate (every 15 m).

907

Figure A2: σ_{tur} versus σ_{tot} diagram with corresponding σ_{psd} based on Eq. A2.

Data Availability Statement.

KASPR and sounding data used in this study are available at Stony Brook University Academic Commons Repository (https://commons.library.stonybrook.edu/somasdata/17). Those data collected under IMPACTS are also available at the NASA Global Hydrometeorology Resource Center (GHRC) DAAC system (http://dx.doi.org/10.5067/IMPACTS/RADAR/DATA101, http://dx.doi.org/10.5067/IMPACTS/SOUNDING/DATA301).

928

References

Benjamin, S. G., S. S. Weygandt, J. M. Brown, M. Hu, C. R. Alexander, T. G. Smirnova, J. B. Olson, E. P. James, D. C. Dowell, G. A. Grell, H. Lin, S. E. Peckham, T. L. Smith, W. R. Moninger, J. S. Kenyon, and G. S. Manikin, 2016: A North American Hourly Assimilation and Model Forecast Cycle: The Rapid Refresh. *Monthly Weather Review* 144, 4, 1669-1694, https://doi.org/10.1175/MWR-D-15-0242.1

Bluestein, H. B., 1993: Observations and Theory of Weather Systems. Vol. 2, Synoptic-Dynamic Meteorology in Midlatitudes. Oxford University Press, 608 pp.

Bosart, L. F., and F. Sanders, 1986: Mesoscale Structure in the Megalopolitan Snowstorm of 11–12 February 1983. Part III: A Large-Amplitude Gravity Wave. J. Atmos. Sci., 43, 924- 939, https://doi.org/10.1175/1520-0469(1986)043<0924:MSITMS>2.0.CO;2.

Boucher, R. J., R. Wexler, D. Atlas, and R. M. Lhermitte, 1965: Mesoscale wind structure revealed by Doppler Radar. J. Appl. Meteor., 4, 590-597.

Browning, K. A., and R. Wexler, 1968: The determination of kinematic properties of a wind field using Doppler radar. J. Appl. Meteorol., 7, 105–113, doi: 10.1175/1520-0450(1968)007<0105:TDOKPO>2.0.CO;2.

Bryan, G. H., J. M. Fritsch, 2000: Moist Absolute Instability: The Sixth Static Stability State. Bull. Amer. Meteor. Soc., 81, 1207–1230.

Byrd, G. P., 1989: A Composite Analysis of Winter Season Overrunning Precipitation Bands over the Southern Plains of the United States. J. Atmos. Sci., 46, 1119–1132, https://doi.org/10.1175/1520-0469(1989)046<1119:ACAOWS>2.0.CO;2.

Colle, B. A., D. Stark, and S. E. Yuter, 2014: Surface microphysical observations within East Coast winter storms on Long Island, New York. Mon. Wea. Rev., 142, 3126–3146, doi:10.1175/MWR-D-14-00035.1.

Cooper, K. B. and G. Chattopadhyay, 2014: Submillimeter-Wave Radar: Solid-State System Design and Applications, in IEEE Microwave Magazine, vol. 15, no. 7, pp. 51-67, Nov.-Dec. 2014, doi: 10.1109/MMM.2014.2356092.

Crawford, A. D., E. A. P. Schreiber, N. Sommer, M. C. Serreze, J. C. Stroeve, and D. G. Barber, 2021: Sensitivity of Northern Hemisphere Cyclone Detection and Tracking Results to Fine Spatial and Temporal Resolution Using ERA5. Mon. Wea. Rev., 149, 2581–2598, https://doi.org/10.1175/MWR-D-20-0417.1.

Doviak, R. J., and D. S. Zrnic (2006): Doppler radar and weather observations, 2nd ed., San Diego, Academic Press, Second Addition. Submillimeter-Wave Radar: Solid-State System Design and Applications

962   Dunnavan, E. L., 2021: How Snow Aggregate Ellipsoid Shape and Orientation Variability Affects Fall
963   Speed and Self-Aggregation Rates. J. Atmos. Sci., 78, 51–73.

964   Ganetis, S. A., B. A., Colle, S. E. Yuter, and N. P. Hoban, 2018: Environmental Conditions Associated with
965   Observed Snowband Structures within Northeast U.S. Winter Storms, Monthly Weather Review Vol.
966   146, No. 11, pp 3675, 1520-0493

967   Hersbach, H., B. Bell, P. Berrisford, S. Hirahara, A. Horányi, J. Muñoz-Sabater, J. Nicolas, C. Peubey,
968   R. Radu, D. Schepers, A. Simmons, C. Soci, S. Abdalla, X. Abellan, G. Balsamo, P. Bechtold, G.
969   Biavati, J. Bidlot, M. Bonavita, G. De Chiara, P. Dahlgren, D. Dee, M. Diamantakis, R. Dragani, J.
970   Flemming, R. Forbes, M. Fuentes, A. Geer, L. Haimberger, S. Healy, R. J. Hogan, E. Hólm, M.
971   Janisková, S. Keeley, P. Laloyaux, P. Lopez, C. Lupu, G. Radnoti, P. de Rosnay, I. Rozum, F.
972   Vamborg, S. Villaume, J.-N. Thépaut: 2020 The ERA5 global reanalysis. Q J R Meteorol Soc., 146,
973   1999– 2049. https://doi.org/10.1002/qj.3803

974   Jurewicz, M. L., Sr., and M. S. Evans, 2004: A comparison of two banded, heavy snowstorms with very
975   different synoptic settings. Wea. Forecasting, 19, 1011-1028, https://doi.org/10.1175/WAF-823.1.

976   Keeler, J. M., B. F. Jewett, R. M. Rauber, G. M. McFarquhar, R. M. Rasmussen, L. Xue, C. Liu, and G.
977   Thompson, 2016a: Dynamics of cloud-top generating cells in winter cyclones. Part I: Idealized
978   simulations in the context of field observations. J. Atmos. Sci., 73, 1507–1527,
979   https://doi.org/10.1175/JAS-D-15-0126.1.

980   Keeler, J. M., B. F. Jewett, R. M. Rauber, G. M. McFarquhar, R. M. Rasmussen, L. Xue, C. Liu, and G.
981   Thompson, 2016b: Dynamics of cloud-top generating cells in winter cyclones. Part II: Radiative and
982   instability forcing. J. Atmos. Sci., 73, 1529–1553, https://doi.org/10.1175/JAS-D-15-0127.1.

983   Keeler, J. M., B. F. Jewett, R. M. Rauber, G. M. McFarquhar, R. M. Rasmussen, L. Xue, C. Liu, and G.
984   Thompson, 2017: Dynamics of cloud-top generating cells in winter cyclones. Part III: Shear and
985   convective organization. J. Atmos. Sci., 74, 2879-2897, https://doi.org/10.1175/JAS-D-16-0314.1.

986   Kollias, P., N. Bharadwaj, K. Widener, I. Jo, and K. Johnson, 2014: Scanning ARM cloud radars. Part I:
987   Operational sampling strategies. Journal of Atmospheric and Oceanic Technology, 31(3), 569– 582

988   Kollias, P., E. Luke, M. Oue, and K. Lamer, 2020: Agile adaptive radar sampling of fast-evolving
989   atmospheric phenomena guided by satellite imagery and surface cameras. Geophysical Research Letters,
990   45, e2020GL088440. https://doi.org/10.1029/2020GL088440

991   Kumjian, M. R., and K. A. Lombardo, 2017: Insights into the Evolving Microphysical and Kinematic
992   Structure of Northeastern U.S. Winter Storms from Dual-Polarization Doppler Radar, Monthly Weather
993   Review, 145(3), 1033-1061.

Kumjian, M. R., S. A. Rutledge, R. M. Rasmussen, P. C. Kennedy, and M. Dixon, 2014: High-resolution polarimetric radar observations of snow-generating cells. J. Appl. Meteor. Climatol., 53, 1636-1658, https://doi.org/10.1175/JAMC-D-13-0312.1.

Kumjian, M. R., D. M. Tobin, M. Oue, and P. Kollias, 2020: Microphysical Insights into Ice Pellet Formation Revealed by Fully Polarimetric Ka-band Doppler Radar. J. Appl. Meteor. Climatol., doi: https://doi.org/10.1175/JAMC-D-20-0054.1

Lackmann, G. M., and G. Thompson, 2019: Hydrometeor Lofting and Mesoscale Snowbands. Mon. Wea. Rev., 147, 3879-3899, https://doi.org/10.1175/MWR-D-19-0036.1.

Lamer, K., M. Oue, A. Battaglia, R. J. Roy, K. B. Cooper, R. Dhillon, and P. Kollias, 2021: Multifrequency radar observations of clouds and precipitation including the G-band, Atmos. Meas. Tech., 14, 3615–3629, https://doi.org/10.5194/amt-14-3615-2021.

Markowski, P. M., and Y. P. Richardson, 2010: Mesoscale Meteorology in Midlatitudes.Wiley-Blackwell, 424 pp.

McMurdie, L. A., G. M. Heymsfield, J. E. Yorks, S. A. Braun, G. Skofronick-Jackson, R. M. Rauber, S. Yuter, B. Colle, G. M. McFarquhar, M. Poellot, D. R. Novak, T. J. Lang, R. Kroodsma, M. McLinden, M. Oue, P. Kollias, M. R. Kumjian, S. J. Greybush, A. J. Heymsfield, J. A. Finlon, V. L. McDonald, and S. Nicholls, 2022: Chasing Snowstorms: The Investigation of Microphysics and Precipitation for Atlantic Coast-Threatening Snowstorms (IMPACTS) Campaign, Bulletin of the American Meteorological Society, 103, pp E1248, 1520-0477.

Molthan, A. L., B. A. Colle, S. E. Yuter, and D. Stark, 2016: Comparisons of Modeled and Observed Reflectivities and Fall Speeds for Snowfall of Varied Riming Degrees during Winter Storms on Long Island, New York, Monthly Weather Review Vol. 144, No. 11, pp 4327, 1520-0493

Morales, R. F., Jr., 2008: The historic Christmas 2004 south Texas snow event: Diagnosis of the heavy snow band. Natl. Wea. Dig., 32, 135–152, http://nwafiles.nwas.org/digest/papers/2008/Vol32No2/Pg135-Morales.pdf.

Naeger, A. R., B. A. Colle, and A. Molthan, 2017: Evaluation of Cloud Microphysical Schemes for a Warm Frontal Snowband during the GPM Cold Season Precipitation Experiment (GCPEx). Mon. Wea. Rev., 145, 4627–4650, https://doi.org/10.1175/MWR-D-17-0081.1.

Naeger, Aaron R., B. A. Colle, N. Zhou, and A. Molthan, 2020: Evaluating Warm and Cold Rain Processes in Cloud Microphysical Schemes Using OLYMPEX Field Measurements, Monthly Weather Review Vol. 148, No. 5, pp 2163, 1520-0493

Novak, D. R., L. F. Bosart, D. Keyser, and J. S. Waldstreicher, 2004: An observational study of cold season-banded precipitation in Northeast U.S. cyclones. Wea. Forecasting, 19, 993-1010, https://doi.org/10.1175/815.1.

1028 Novak, D. R., B. A. Colle, and A. Aiyyer, 2010: Evolution of mesoscale precipitation band environments
1029   within the comma head of northeast U.S. cyclones. Mon. Wea. Rev., 138, 2354–2374.

1030 Novak, D. R., B. A. Colle, and S. E. Yuter, 2008: High-Resolution Observations and Model Simulations of
1031   the Life Cycle of an Intense Mesoscale Snowband over the Northeastern United States. Mon. Wea. Rev.,
1032   136, 1433–1456, https://doi.org/10.1175/2007MWR2233.1.

1033 Oue, M., P. Kollias, E. P. Luke, A. Ryzhkov, 2017: A New Ka-Band Scanning Radar Facility: Polarimetric
1034   and Doppler Spectra Measurements of Snow Events. AGU Fall Meeting, A31G-2270, New Orleans 11-
1035   15 December, 2017.

1036 Oue, M., Kollias, P., Matrosov, S. Y., Battaglia, A., and Ryzhkov, A. V., 2021: Analysis of the
1037   microphysical properties of snowfall using scanning polarimetric and vertically pointing multi-
1038   frequency Doppler radars, Atmos. Meas. Tech., 14, 4893–4913, https://doi.org/10.5194/amt-14-4893-
1039   2021.

1040 Petterssen, S., 1956: Motion and Motion Systems. Vol. 1, Weather Analysis and Forecasting, 2nd ed.,
1041   McGraw Hill, 428 pp.

1042 Plummer, D. M., G. M. McFarquhar, R. M. Rauber, B. F. Jewett, and D. Leon, 2014: Structure and
1043   statistical analysis of the microphysical properties of generating cells in the comma-head region of
1044   continental winter cyclones. J. Atmos. Sci., 71, 4181-4203, https://doi.org/10.1175/JAS-D-14-0100.1.

1045 Plummer, D. M., G. M. McFarquhar, R. M. Rauber, B. F. Jewett, and D. C. Leon, 2015: Microphysical
1046   properties of convectively generated fall streaks within the stratiform comma head region of continental
1047   winter cyclones. J. Atmos. Sci., 72, 2465–2483, https://doi.org/10.1175/JAS-D-14-0354.1.

1048 Protat, A., and C. R. Williams, 2011: The Accuracy of Radar Estimates of Ice Terminal Fall Speed from
1049   Vertically Pointing Doppler Radar Measurements. Journal of Applied Meteorology and Climatology,
1050   50(10), 2120–2138.

1051 Rauber, R. M., J. Wegman, D. M. Plummer, A. A. Rosenow, M. Peterson, G. M. McFarquhar, B. F. Jewett,
1052   D. Leon, P. S. Market, K. R. Knupp, J. M. Keeler, and S. M. Battaglia, 2014: Stability and charging
1053   characteristics of the comma head region of continental winter cyclones. J. Atmos. Sci., 71, 1559-1582,
1054   https://doi.org/10.1175/JAS-D-13-0253.1.

1055 Rauber, R. M., S. M. Ellis, J. Vivekanandan, J. Stith, W-C Lee, G. M. McFarquhar, and B. F. Jewett, 2017:
1056   Finescale structure of a snowstorm over the Northeastern United States: a first look at high resolution
1057   HIAPER Cloud Radar Observations. Bull. Amer. Meteor. Soc., 98, 253-269,
1058   https://doi.org/10.1175/BAMS-D-15-00180.1.

1059 Reuter, G. W., and M. K. Yau, 1990: Observations of Slantwise Convective instability in Winter Cyclones.
1060   Mon. Wea. Rev., 118, 447–458, https://doi.org/10.1175/1520-
1061   0493(1990)118<0447:OOSCII>2.0.CO;2.

Reges, H. W., N. Doesken, J. Turner, N. Newman, A. Bergantino, and Z. Schwalbe, 2016: CoCoRaHS: The evolution and accomplishments of a volunteer rain gauge network. Bull. Amer. Meteor. Soc., 97, 1831–1846, https://doi.org/10.1175/BAMS-D-14-00213.1.

Rosenow, A. A., D. M. Plummer, R. M. Rauber, G. M. McFarquhar, B. F. Jewett, and D. Leon, 2014: Vertical Velocity and Physical Structure of Generating Cells and Convection in the Comma Head Region of Continental Winter Cyclones. J. Atmos. Sci., 71, 1538–1558. https://doi.org/10.1175/JAS-D-13-0249.1.

Rosenow, A.A., R.M. Rauber, G.M. McFarquhar and J.M. Keeler, 2018: Elevated potential instability in the comma-head: Distribution and development. Mon. Wea. Rev., 146, 1259-1278. https://doi.org/10.1175/MWR-D-17-0283.1.

Schmidt, J.M., P. J. Flatau, P. R. Harasti, R. D. Yates, R. Littleton, S. Pritchard, J. M. Fischer, E. J. Fischer, W. J. Kohri, J. R. Vetter, S. Richman, D. B. Baranowski, M. J. Anderson, Ed. Fletcher, and D. W. Lando, 2012: Radar observations of individual rain drops in the free atmosphere. Proceeding of the National Academy Sciences of the United States of America. 109, 9293–9298. www.pnas.org/cgi/doi/10.1073/pnas.1117776109

Schultz, D. M., and J. A. Knox, 2007: Banded Convection Caused by Frontogenesis in a Conditionally, Symmetrically, and Inertially Unstable Environment, Mon. Wea. Rev., 135(6), 2095-2110, https://doi.org/10.1175/MWR3400.1.

Schultz, D. M., and P. N. Schumacher, 1999: The Use and Misuse of Conditional Symmetric Instability, Mon. Wea. Rev., 127, 2709-2732, https://doi.org/10.1175/1520-0493(1999)127<2709:TUAMOC>2.0.CO;2.

Stark, D., B. A. Colle, and S. E. Yuter, 2013: Observed microphysical evolution for two East Coast winter storms and the associated snow bands. Mon. Wea. Rev., 141, 2037–2057, doi:10.1175/MWR-D-12-00276.1.

Syrett, W.J., B.A. Albrecht, and E.E. Clothiaux, 1995: Vertical Cloud Structure in a Midlatitude Cyclone from a 94-GHz Radar. Mon. Wea. Rev., 123, 3393–3407

Trapp, J. R., D. M. Schultz, A. V. Ryzhkov, and R. L. Holle, 2001: Multiscale structure and evolution of an Oklahoma winter precipitation event. Mon. Wea. Rev., 129, 486–501, https://doi.org/10.1175/1520-0493(2001)129<0486:MSAEOA>2.0.CO;2.

Wexler, R., A. C. Chmela, and G. M. Armstrong, 1967: Wind field observations by Doppler radar in a New England snowstorm. Mon. Wea. Rev, 95, 929-935

Xu, Q., 1992: Formation and evolution of frontal rainbands and geostrophic potential vorticity anomalies. J. Atmos. Sci., 49, 629–648.

1095   Zhang, F., S. E. Koch, C. A. Davis, and M. L. Kaplan, 2001: Wavelet analysis and the governing dynamics

1096   of a large-amplitude gravity wave event along the East Coast of the United States. Quart. J. Roy. Meteor.

1097   Soc., 127, 2209–2245.

1098   Zhang, F., C. Synder, and R. Rotunno, 2003: Effects of moist convection on mesoscale predictability. J.

1099   Atmos. Sci., 60, 1173–1185.

1100